Control Engineering Practice 135 (2023) 105492

Contents lists available at ScienceDirect

Control Engineering Practice

journal homepage: www.elsevier.com/locate/conengprac

A distributed relative localization approach for air-ground robot formations with onboard sensing

Samet Güler [a,*], İsa E. Yıldırım [b]

[a] Faculty of Engineering, Abdullah Gül University, Barbaros, Kayseri, 38080, Turkey
[b] Graduate School of Engineering and Science, Abdullah Gül University, Barbaros, Kayseri, 38080, Turkey

ARTICLE INFO

Keywords:
Multi-robot systems
Localization
Ultrawideband sensing
Estimation

ABSTRACT

In a multi-robot system, diversity in the sensing and motion models of robotic entities can improve the overall performance. While such heterogeneous systems offer peculiar advantages in terms of robustness and resiliency, positioning and situational awareness of individual robots in these systems remain a challenge. In this paper, the problem of relative localization in a system composed of a drone and multiple unmanned ground vehicles which are desired to move in formation is addressed. By utilizing a leader–follower formation graph, a distance-based relative localization algorithm based on an extended Kalman filter is proposed for online estimation of the relative positions among the ground vehicles. The necessary conditions to satisfy the observability of the unmeasured states are provided. In the proposed framework, the robots exchange a limited amount of information only and do not rely on an external infrastructure, GPS, or magnetometer. Furthermore, an application of the proposed localization framework integrated to custom formation control schemes is proposed. The performance of the proposed approach is evaluated through a set of simulation and real life experiments, and its advantages and limitations are discussed by means of a comparative study.

1. Introduction

Heterogeneity of robotic entities in a multi-robot system provides unique advantages in terms of both high-level task allocation and low-level control mechanisms. A team of air and ground robots can exploit their distinct sensing and motion capabilities to achieve robustly demanding objectives such as 3D mapping, search and rescue, and border patrolling (Kushleyev et al., 2013). To enable the implementation of such applications with heterogeneous multi-robot systems (HMRS), different software architectures of individual robots can be unified under the Robot Operating System (ROS) middleware. The following example emphasizes the unique synergy between the air and ground components in a robot team. Consider an agricultural field which needs to be covered by a team of ground robots collaboratively for detection of plant malfunctions or disinfection. There might be some environmental constraints ahead of the team which may not be detected at the height of the ground robots such as obstacles or an uneven terrain. How can this objective be achieved reliably? What sort of path planning algorithms can be applied for the robot team? In such scenarios, a solution would be to integrate a vision-aided drone to the formation such that it flies in coordination with the UGV team and can reactively redesign the path of the entire formation. Also, the drone can help ground robots to maintain a desired formation by acting as a flying leader. Similar advantages and characteristics of HMRS can be found in the comprehensive survey (Liu et al., 2022).

While HMRS can yield better performance and resiliency in many duties compared to robot teams of homogeneous entities, the relative localization and distributed formation control of HMRS remains an open problem. A primary approach for finding the relative locations between team members is to employ absolute sensors such as GPS and motion capture (mocap) systems for acquiring the positions of individual robots. Then, the acquired data can be post-processed to compute the relative positions between the robots. Although this approach can provide high performance in some settings, it does not offer a universal solution because such absolute sensors yield accurate position data in certain environments only. Particularly, GPS does not function indoors, and mocap systems limit the configuration space of the robots. Since many distributed formation control algorithms rely on the existence of relative positions between robots, each robot in an HMRS should be equipped with onboard sensors for reliable relative localization in all environments.

In general, the characteristics of the onboard sensors utilized shape the design process of a localization framework. Notably, some sensors may yield unreliable readings in some environments. For instance, magnetometer sensors are highly affected by the existence of nearby metallic objects, which restricts the type of the operation environment.

* Corresponding author.
E-mail address: samet.guler@agu.edu.tr (S. Güler).

https://doi.org/10.1016/j.conengprac.2023.105492
Received 15 December 2022; Received in revised form 4 March 2023; Accepted 7 March 2023
Available online 20 March 2023

Also, the performance of vision sensors depend greatly on the ambient conditions, which can degrade the multi-robot localization performance significantly in uncertain environments. Recently, the ultrawideband (UWB) sensor technology has been utilized for multi-robot localization. A pair of UWB sensors communicate at certain frequencies to generate peer-to-peer distance measurements by applying the time-of-flight (ToF) technique. In contrast to the vision and ultrasonic sensors, UWB radio sensors can produce reliable, omnidirectional distance measurements continuously at varying angle configurations. They can provide a satisfactory level of accuracy for distances of up to tens of meters. All these properties make the UWB sensors an appropriate option for multi-robot localization.

To address the aforementioned challenges, in this work the relative localization objective is studied for a team composed of a drone carrying an onboard monocular camera and multiple unmanned ground vehicles (UGV) with ultrawideband (UWB) sensors. An extended Kalman filter fuses the onboard sensor measurements and communicated variables to estimate online the relative positions between the UGVs. Particularly, the drone is commanded to track a leader UGV to provide the UGVs with the distance measurements required for estimation. Furthermore, to handle the observability issue arising from the distance-only estimation mechanism, a complementary formation controller which satisfies the observability constraints on the velocity is proposed. Several successful simulation and experimental results with varying numbers of UGVs are presented.

The leader–follower formation architectures are shown to demonstrate better performance in multi-robot system implementations compared to the centralized architectures (such as virtual leader approach) in terms of scalability and robustness. Thus, a leader–follower architecture is employed, where a drone acts as a coleader by cooperating in the relative localization task within the UGV team. Particularly, the drone carries a UWB sensor at a certain configuration in the formation to generate the relative position estimations. In contrast to the previous works where the required number of drones increases with the addition of each UGV in the team, single drone suffices for the estimation task in the proposed framework. In addition, the proposed drone configuration has the potential of facilitating the design of further online formation path planners.

The main contributions of the work are three-fold:

- A relative localization framework for an air-ground robot team with onboard distance sensors is proposed. Since the proposed framework does not depend on a fixed infrastructure or magnetometer sensor, the HMRS can function in environments with unreliable magnetic field or weak GPS signals.
- Vision-based relative localization approaches require the UGVs to always reside in the camera images of the aerial vehicles, which may result in tight formations with inter-robot distances of less than one meter. Utilizing UWB distance sensors in a leader–follower formation, the proposed framework increases the allowable inter-robot distances and removes the tight UGV formation requirement.
- It is shown that the relative bearing angles between the UGVs remain observable under mild assumptions, which is crucial for teams with minimal onboard sensing capabilities. With two formation control frameworks designed to guarantee the observability of the unmeasured states, the applicability of the system in real life conditions is demonstrated through several experiments.

The rest of the work is organized as follows. After presenting an overview of some related works in Section 2, Section 3 defines the HMRS model and formulates the localization problem. In Section 4, the UWB ranging and calibration scheme is explained. In Section 5, the filtering algorithm and estimation framework are proposed, and the observability of the system states is analyzed. In Section 6, two custom formation control algorithms are designed to be used with the proposed estimation framework. Sections 7 and 8 demonstrate the simulation and experimental results. In Section 9, the proposed design is compared with the previous works with a detailed discussion. Finally, Section 10 concludes the work.

2. Related work

The unique benefits of HMRS have been demonstrated in a collection of papers. Staub et al. (2017) combines the flexible workspace feature of drones with the high payload capability of mobile manipulators and propose a system of a mobile manipulator and a drone for transporting rigid objects. As reported in Tokekar et al. (2016), intermittent transfer of aerial robots by ground robots can extend the functionalities of HMRS. Manyam et al. (2016) studies the path planning problem for a UGV and an unmanned aerial vehicle (UAV) such that every target position is visited by at least one of the team members. Grocholsky et al. (2006), Vidal et al. (2002), Yu et al. (2015) emphasize the importance of mixed UAV/UGV teams for the target detection and tracking problem. Cognetti et al. (2014) designs an optimal controller for a HMRS to follow a desired volume while avoiding obstacles. Remarkable advantages of the heterogeneous sensing capabilities have been further explored in Kaslin et al. (2016), Li et al. (2016), Mueggler et al. (2014). Moreover, the peculiar features of HMRS are demonstrated in some leading robotics competitions. For instance, a part of the 2020 Mohamed bin Zayed International Robotics Competition (MBZIRC) consisted of the task of transporting brick walls to a desired region and stacking them by a team of drones and mobile manipulators (MBZIRC, 2017).

The synergy between the air and ground teams to accomplish such tasks can be built with a reliable relative localization framework only. In the last decade, several types of sensors have been fused on robots to solve the relative localization problem in MRS. Previous approaches can be classified as distance-based and vision-based. Typically, distance sensors are fused with proprioceptive sensors such as IMU in a centralized (Kia et al., 2016; Kim & Kim, 2013) or distributed (Güler et al., 2019, 2018; Hepp et al., 2016; Prorok et al., 2011; Wallar et al., 2018) manner. While ultrasonic or laser range sensors provide limited field-of-view (FOV), Bluetooth, Wi-Fi, and ultrawideband (UWB)-based sensors can generate omnidirectional range data. Although the received-signal-strength (RSS) based range calculation can yield low signal-to-noise-ratio in Bluetooth and WiFi sensors, time-of-flight (TOF)-based UWB sensors provide high accuracy and precision in several challenging scenarios (Güler et al., 2019, 2018; Hepp et al., 2016; Wallar et al., 2018). The communication-free frameworks in Güler et al. (2019, 2018), Hepp et al. (2016) sufficed to realize the basic formation control algorithms which are independent of external localization infrastructures.

Essentially, distance-based approaches take advantage of the Euclidean geometry to extract relations between the swarm members. Cornejo and Nagpal (2015) provide a complete roadmap for range-based relative localization by using geometrical relations and odometry data. However, the lack of evaluations makes its applicability debatable. Cao et al. (2018), Klingner et al. (2019) study the collaborative localization problem on an arbitrary number of ground robots equipped with IR and UWB sensors, respectively. While their solution can be promising for large robot swarms, they require the robots to be stationary for a certain time interval. Also, the simulation studies of Cao et al. (2018) ignore the UWB sensor characteristics which can have significant effects, particularly in mesh networks.

On the other hand, vision sensors provide extensive information about a robot's environment, but processing and interpreting the acquired data remain a fundamental challenge. Cognetti et al. (2014), Krajník et al. (2014), Roelofsen et al. (2015), Saska et al. (2016) used tags with specific patterns on robots which move in leader–follower formations to calculate the relative positions. Later, the same objective was achieved with deep learning methods by removing the need for onboard tags at the expense of increased computational complexity (Kabore & Guler, 2021; Vrba & Saska, 2020). High detection rates with the convolutional neural network (CNN) methods are reported in several tasks. However, with vision-only approaches, the inter-robot ranges are estimated by projecting the 2D image to 3D, which can result in poor performance as compared to UWB ranging.

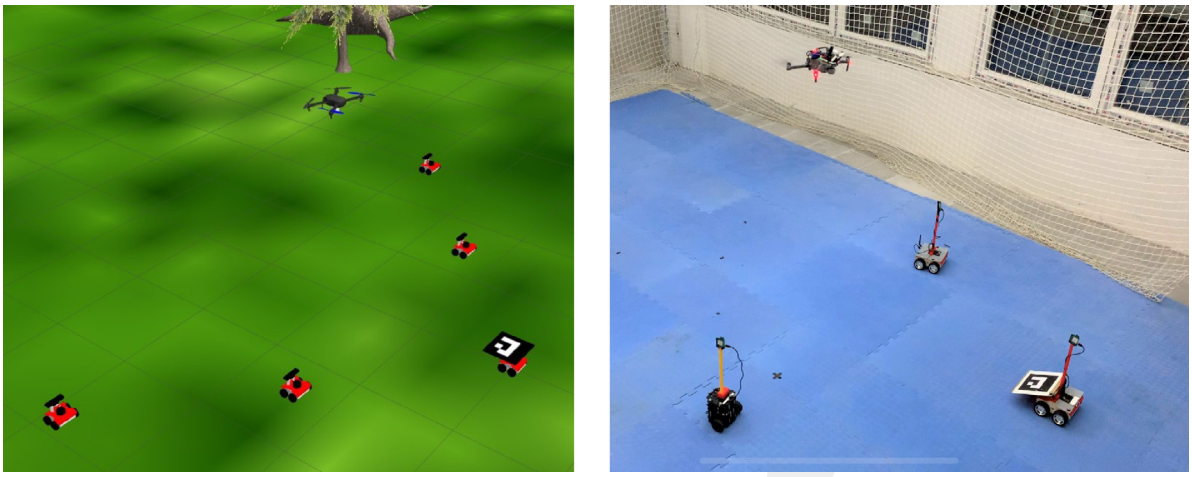

(a) (b)

Fig. 1. (a) A sample heterogeneous team composed of five UGVs and a drone; (b) an experimental setup including three UGVs and a drone.

The proposed approach differs from the aforementioned works in the sense that it aims at improving the situational awareness of the robots in HMRS and focuses on relative localization by fusing the onboard distance and vision sensing modalities. Also, in Grocholsky et al. (2006), Manyam et al. (2016), Staub et al. (2017), Tokekar et al. (2016), Vidal et al. (2002), Yu et al. (2015), the main objectives are path planning, map building or target tracking with some localization infrastructure aids, which limit their application areas to certain environments. Moreover, unlike Güler et al. (2022), no magnetometer sensor is utilized, and thus the entire team is not restricted to a fixed frame. While Cognetti et al. (2014) proposes a complete perception-decision framework for air-ground teams, they restrict the formation such that every ground robot should be covered by the vision sensors of at least one aerial vehicle. In the proposed framework, the only condition on the robot formation is that the leader UGV should be followed by the drone, while the other UGVs can be positioned at large inter-robot distances within the UWB sensor limitations.

3. Problem formulation

Consider a heterogeneous multi-robot system (HMRS) $\mathcal{M}$ consisting of $N+1$ non-holonomic unmanned ground vehicles (UGV) R_i and an unmanned aerial vehicle (UAV) D_0 which seek to move in coordination to accomplish a given objective. The motion model of a UGV R_i is represented as the usual non-holonomic kinematics as follows:

$$\dot{\mathbf{p}}_i = \left[\cos(\theta_i), \sin(\theta_i)\right]^\top v_i, \tag{1}$$

$$\dot{\theta}_i = \omega_i, \tag{2}$$

where $\mathbf{p}_i = \left[x_i, y_i\right]^\top \in \Re^2$ is the 2D position, $\theta_i \in [-\pi, \pi)$ is the heading angle with respect to a fixed frame $\mathcal{F}_\mathrm{G}$, and v_i, ω_i are the linear and angular speed commands of R_i, $i \in \{0, \dots, N\}$. Typically, the velocity inputs of a UGV are bounded due to physical limitations. Thus, it is assumed that

$$|v_i(t)| \le \bar{v}_i, \ |\omega_i(t)| \le \bar{\omega}_i \quad \forall t \ge t_0, \ \forall i \in \{0, \dots, N\}, \tag{3}$$

for some arbitrary $\bar{v}_i > 0$ and $\bar{\omega}_i > 0$. In addition, to satisfy a smooth trajectory for the entire formation, it is assumed that

$$v_0(t) \ge 0, \quad r_\mathrm{turn} = \frac{|v_0(t)|}{|\omega_0(t)|} \ge \bar{r}_\mathrm{turn}, \tag{4}$$

where r_turn is the turning radius of R_0 and $\bar{r}_\mathrm{turn}$ is a constant design parameter which needs to be chosen such that the leader robot is not allowed to make sharp turns. Notably, this assumption is natural in practical realization of formations of nonholonomic UGVs (Liu et al., 2022; Saska et al., 2014).

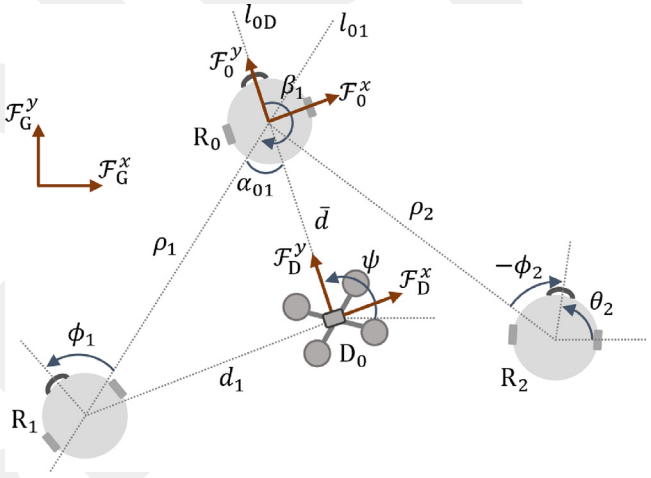

Fig. 2. A top view of the proposed localization graph among a team of three UGVs and a drone, projected onto a 2D plane. Both the global frame $\mathcal{F}_\mathrm{G}$ and the local frame of the drone $\mathcal{F}_\mathrm{D}$ are shown with red arrows. The heading angle θ_2 of robot R_2 with respect to $\mathcal{F}_\mathrm{G}$ and the relative heading angles ϕ_1, ϕ_2 are also presented. (For interpretation of the references to color in this figure legend, the reader is referred to the web version of this article.)

Essentially, the dynamics of a UAV is modeled as a 6-DOF rigid body moving in 3D space, consisting of three linear velocity terms (x, y, z) and three angular velocity terms (roll, pitch, yaw). The drone is considered to be a vertical take-off-and-landing (VTOL) UAV which flies at an altitude $\bar{h} \in \{h_\mathrm{min}, h_\mathrm{max}\}$ from the ground, where the design parameters $h_\mathrm{max} > h_\mathrm{min} > 0$ can be chosen based on the UAV type. Also, it is assumed that the motion in the roll and pitch axes are stabilized by a low-level controller which can be achieved by most commercial autopilots. Thus, the state vector of D_0 is defined by $\zeta = \left[x_D, y_D, \psi\right]^\top \in \Re^3$, where $\mathbf{p}_D = \left[x_D, y_D\right]^\top$ is the 2D coordinate vector and $\psi \in [-\pi, \pi)$ is the heading angle with respect to the fixed frame $\mathcal{F}_\mathrm{G}$.

Among the HMRS, an underlying localization graph $\mathcal{G}(\mathcal{V}, \mathcal{E})$ with the node set $\mathcal{V}$ and the edge set $\mathcal{E}$ is defined. UGV R_0 is assigned as the leader robot which moves with a predefined path planning procedure. The other UGVs R_i, $i \in \{1, \dots, N\}$, and drone D_0 are assigned as the first followers which aim to follow the leader R_0. Such a structure results in a directed leader-first follower graph with the edge set $\mathcal{E} = \left\{(v_1, v_0), \dots, (v_N, v_0), (v_\mathrm{D}, v_0)\right\}$, where the nodes v_i, $i \in \{0, \dots, N\}$, and v_D represent the UGVs R_i, $i \in \{0, \dots, N\}$, and drone D_0, respectively (Fig. 2). Referring to Fig. 2, let $\rho_i = \|\mathbf{p}_i - \mathbf{p}_0\|$ and $\beta_i \in [-\pi, \pi)$ denote the

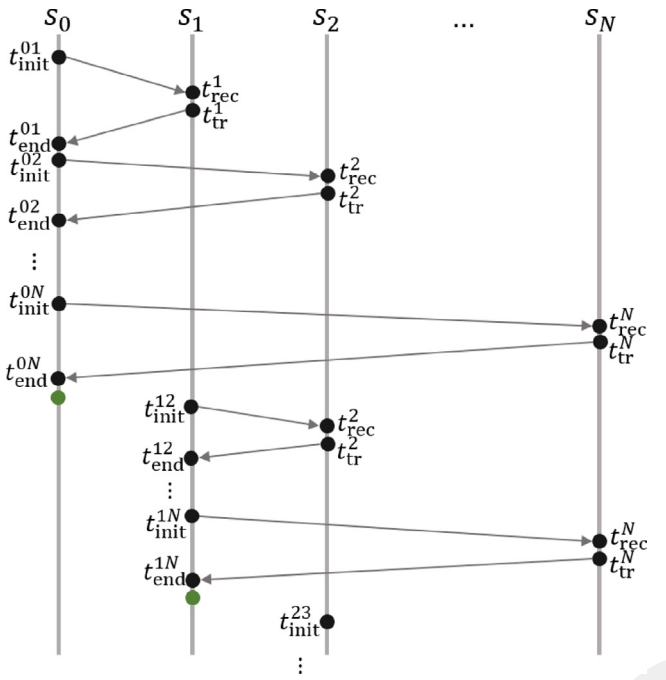

Fig. 3. The UWB timing scheme among the $N+1$ sensors $s_i,\ i \in \{0,\dots,N\}$. Each sensor s_i broadcasts a message after sensor s_{i-1} completes its calculations. The message communications are depicted with the directed arrows, and the dots denote the time a message is received or transmitted by a particular sensor.

distance and relative bearing angle between R_0 and $\mathsf{R}_i,\ i \in \{1,\dots,N\}$, respectively. Also, denote by $\phi_i \in [-\pi,\pi)$ the relative heading of $\mathsf{R}_i,\ i \in \{1,\dots,N\}$, calculated counterclockwise from the line segment l_{0i} to the heading of R_i. Finally, let $d_i = \|\mathbf{p}_i - \mathbf{p}_D\|$ denote the distance between D_0 and $\mathsf{R}_i,\ i \in \{1,\dots,N\}$. Remarkably, the variables $\rho_i, d_i, \phi_i, \beta_i$ do not depend on the fixed frame $\mathcal{F}_G$. Denote the sets of the UGVs that reside on the left and right sides of the line l_{0D} by $\mathcal{S}_L$ and $\mathcal{S}_R$, respectively. We have the following assumption.

Assumption 3.1. The UGVs $\mathsf{R}_i \in \mathcal{S}_L$ satisfy $-\pi + \beta_{\text{th}} < \beta_i(t) < \frac{-\pi}{2} - \beta_{\text{th}}$ and the UGVs $\mathsf{R}_j \in \mathcal{S}_R$ satisfy $\frac{\pi}{2} + \beta_{\text{th}} < \beta_j(t) < \pi - \beta_{\text{th}}$, where β_{th} is a design constant. Also, it holds that $d_i(t) > d_{\min},\ i \in \{0,\dots,N\}$, and $\rho_i(t) > \rho_{\min},\ i \in \{1,\dots,N\}$, for some arbitrary $d_{\min}, \rho_{\min} > 0$ and for all $t \geq t_0$.

The constraints on the angles β_i and the distances ρ_i, d_i are required for avoiding collinear robots case and deriving further geometrical relations and can be satisfied by designing the formation configuration accordingly.

The goal is to minimize the number of the sensing and communication units onboard of the robots in the design process. It is assumed that every robot is equipped with a UWB sensor which provides the robots with the inter-robot distance measurements

$$\rho_i(t) = \bar{\rho}_i(t) + \zeta^{\rho}_i(t) \tag{5}$$

$$d_i(t) = \bar{d}_i(t) + \zeta^{d}_i(t) \tag{6}$$

where $\bar{\rho}_i, \bar{d}_i$ are the true distance values and $\zeta^{\rho}_i, \zeta^{d}_i \sim \mathcal{N}(0,\sigma^2_d)$ are zero-mean i.i.d. Gaussian random variables denoting noise. The UWB sensor measurement modeling is discussed explicitly in Section 4. Furthermore, drone D_0 is equipped with a downward-facing monocular camera to track the leader UGV R_0.

With the goal of devising a scalable and robust relative localization framework for $\mathcal{M}$ that enables the realization of the common distributed formation control algorithms, the following objectives are considered:

Objective 1. *Consider the HMRS $\mathcal{M}$ as described in this section. In the absence of an external positioning system or a magnetometer sensor,*

(i) design a relative localization framework for a UGV $\mathsf{R}_i,\ i = (1,\dots,N)$ that estimates its relative configuration toward the leader R_0,

(ii) design a localization and control system for drone D_0 such that it follows the leader R_0 at a certain relative configuration.

Before proposing the localization framework, the UWB sensor characteristics are presented in the following section.

4. UWB sensor measurement modeling

UWB radio technology provides a reliable communication medium across a high bandwidth. A pair of UWB sensors can generate the distance between themselves by communicating at certain time intervals at a large bandwidth and utilizing ranging techniques such as time-of-flight (TOF, also referred to as time-of-arrival (TOA)) and time-difference-of-arrival (TDOA). In the proposed framework, the inter-robot distance measurements are acquired from the UWB sensors mounted on the robots. This section introduces the work mechanism and properties of UWB sensors and our distance measurement acquisition method. Particularly, the Decawave MDEK1001 model is considered, noting that the procedure applies to most of the commercial UWB sensors capable of the TOF-based ranging.

4.1. Ranging method

Inspired by the methodology of Queralta et al. (2022), a single-sided two-way ranging method is applied for distance measurements. Fig. 3 summarizes the ranging mechanism for $N+1$ sensors $s_i,\ i \in \{0,\dots,N\}$ on a vertical time axis. In this figure, the message communications are depicted with the directed arrows, and the dots denote the time a message is received or transmitted. The goal is to generate the distances d_{ij} between each s_i and $s_j,\ i,j \in \{0,\dots,N\}, i \neq j$.

The sensors are modified to execute the following ranging algorithm. First, the initiator sensor s_0 broadcasts a message at time t^{01}_{init}. This message contains certain communication parameters as well as a timestamp in the clock of sensor s_0 and a target sensor identity. Once this message is received by sensor s_1 at time t^{1}_{rec}, it is processed in the sensor's processor within a predefined time. Consequently, sensor s_1 broadcasts a new message with a timestamp indicating the time difference $t^{1}_{\text{tr}} - t^{1}_{\text{rec}}$, which is a summation of the sensor's processing time and the antenna reception and transmission delays. When sensor s_0 receives this message from sensor s_1 at time t^{01}_{end}, it calculates the distance d_{01} as follows:

$$d_{01} = \frac{\left(t^{01}_{\text{end}} - t^{01}_{\text{init}} - \left(t^{1}_{\text{tr}} - t^{1}_{\text{rec}}\right)\right) c}{2} \tag{7}$$

where c is the speed of light on air. Afterwards, sensor s_0 broadcasts a new message at t^{02}_{init} targeting sensor s_2, and the same communication occurs between sensors s_0 and s_2 to generate the distance d_{02}. This ranging algorithm runs sequentially until sensor s_0 calculates the distance d_{0N} to sensor s_N. At this point, sensor s_0 broadcasts an informative message so that all sensors will be informed with the distances $\{d_{01}, d_{02}, \dots, d_{0N}\}$ (presented with the green dot on the first column). Once this message is acquired by sensor s_1, it assumes the initiator role and starts the same procedure to calculate the distances $d_{1j}, j \in \{2,\dots,N\}$ to sensors $s_k, k \in \{2,\dots,N\}$. This procedure is repeated sequentially until sensor s_N becomes the initiator, which terminates the ranging loop and starts a new ranging loop by assigning the initiator role to sensor s_0. As a result of this technique, all distances $d_{ij},\ i,j \in \{0,\dots,N\}, i \neq j$ are calculated at the end of each ranging loop.

With the method described above, a data rate of 10 Hz is obtained for four UWB sensors to generate the six distances between each pair of the sensors. For a three-sensor system, a data rate of 16 Hz is obtained. Fundamentally, the distance data rate is expected to reduce

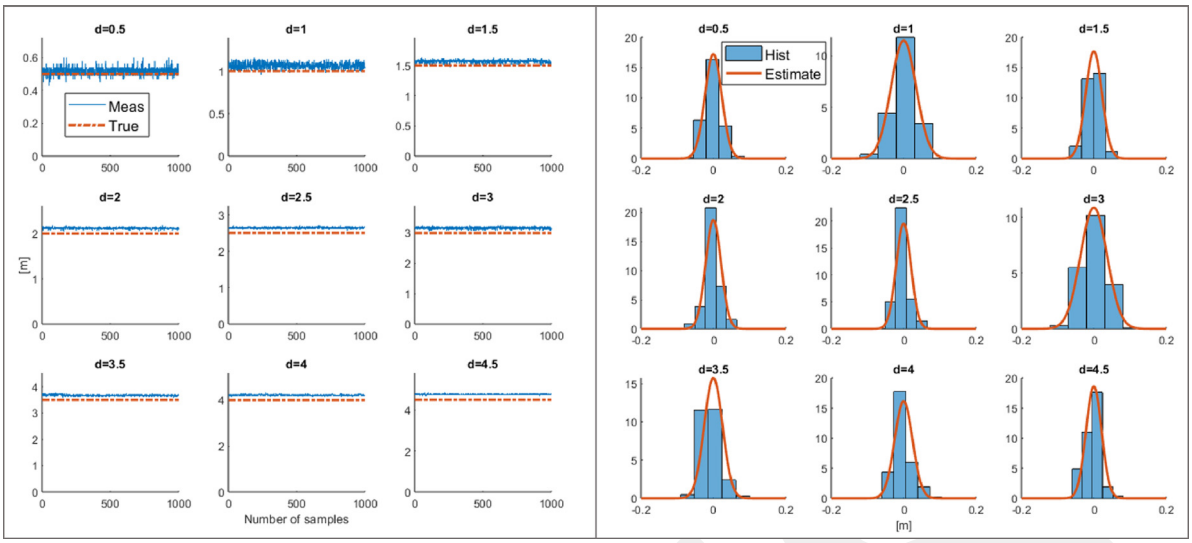

Fig. 4. UWB calibration results: (a) The measurements d^{ij} and true distances $\bar{d}^{ij}$ between two sensors $\{s_i, s_j\}$ at nine different distances $\bar{d}_{ij} = \{0.5, 1, 1.5, \dots, 4, 4.5\}$ m, (b) Noise histograms for the nine distances.

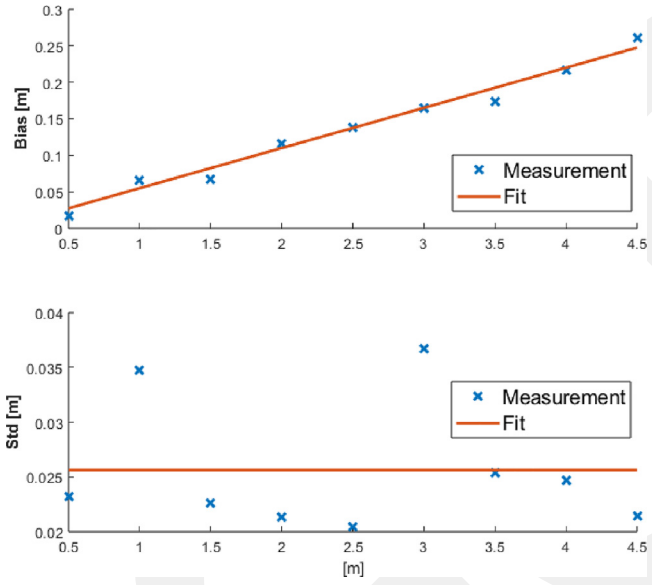

Fig. 5. (Top) The measured biases $b_{ij}(\bar{d}_{ij})$ and its linear fit $b_{ij} = 0.055\bar{d}_{ij}$, and (bottom) the standard deviations σ_{ij} and their mean.

as more sensors are used due to the sequential structure of the proposed mechanism. It is worth to note that the data rate can be improved by reducing the time differences $(t^{i,j+1}_{\text{init}} - t^{i,j}_{\text{end}})$ at the expanse of losing some echoed pulses.

Remarkably, the exact values of t^j_{rec} and t^j_{tr} are not required for calculating the ranges d_{ij} on sensor $s_i, i \neq j$. Only the time difference $\left(t^j_{\text{tr}} - t^j_{\text{rec}}\right)$ is calculated and broadcast by sensor s_j. Therefore, a synchronization procedure among the UWB sensors is not required for this ranging method because only the time differences are utilized in (7).

4.2. Calibration

To mitigate the inaccuracies in the calculated ranges and model the measurement noises, the UWB sensors need to be calibrated. A UWB calibration procedure consists of collecting a dataset and analyzing the measurement signal behavior. Considering the particular scenario of multi-robot localization, we assume that there is no occluding object between the UWB sensors (i.e., between the robots), and study the line-of-sight (LOS) case. The measurement behavior in non-line-of-sight (NLOS) cases differs from the LOS case depending on the material, size, and location of the occluding objects. Thus, the modeling of NLOS scenarios requires more dataset and detailed analysis, which is out of the scope of the current work. The UWB calibration procedure of Guler et al. (2021) is applied. To mitigate the multi-path effects, the sensors are placed in the upright position and 50 cm away from the ground surface (Fig. 13).

First, a pair of sensors $\{s_i, s_j\}$ are chosen, and a dataset of 1000 measurements d_{ij} is recorded at a fixed true distance $\bar{d}_{ij}$ where $\bar{d}_{ij}$ is chosen from the discrete set $\{0.5, 1, 1.5, \dots, 4, 4.5\}$ m in each experiment. Then, for each true distance value $\bar{d}_{ij}$, the noise signal is obtained as follows:

$$\delta_{ij}[k] = d_{ij}[k] - \bar{d}_{ij}[k], \tag{8}$$

where k is the measurement index. The measured distances and their true values in an experiment are illustrated in Fig. 4a. In line with the previous works, it was observed that the noise signal δ_{ij} can be approximated by a Gaussian signal with a mean and standard deviation specific to the true distance values. Thus, the mean of the noise signal is assumed to be the bias b_{ij} which can be approximated by a linear function of the true distance $\bar{d}_{ij}$ (Fig. 5-top). Accordingly, Fig. 4b depicts the resulting signals $\delta_{ij} - b_{ij}$ together with their (zero-mean) Gaussian approximations. It was observed that, to further simplify the analysis, the standard deviation can be approximated by a constant (Fig. 5-bottom). Also, it was found that all pairs of sensors show a similar pattern.

As a result of the above analysis, it is appropriate to assume that the UWB distance measurements can be modeled as

$$d_{ij}[k] = \left(1 + b_{ij}\right) \bar{d}_{ij}[k] + \zeta_{ij}, \tag{9}$$

where $\zeta_{ij} \sim \mathcal{N}(0, \sigma^2_{ij})$ denote the zero-mean i.i.d. Gaussian random variable. Since the bias values are found empirically, one can use $\frac{1}{1+b_{ij}} d_{ij}$ to approximate the true distance. Therefore, in Section 3, the UGV–UGV distances ρ_i and UGV-drone distances d_i are assumed to be contaminated by zero-mean Gaussian noises ζ^ρ_i, ζ^d_i.

A typical UWB sensor pair produce distance measurements that change with the varying antenna directions for the same distance (Jiménez & Seco, 2021; Ledergerber & D'Andrea, 2017). Usually, the fluctuations in the UWB sensor readings are affected by the antenna direction, metallic materials in the environment, and ground separation of the antenna. Consider the UWB sensors s_0 and s_1 mounted on UGVs

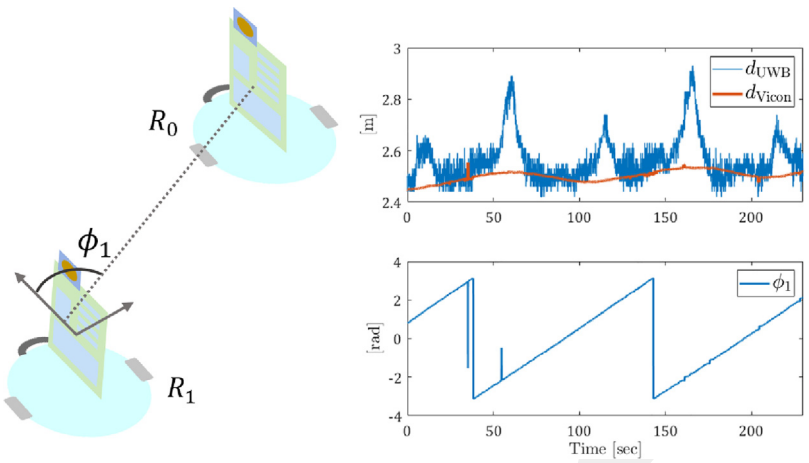

Fig. 6. UWB sensor characteristics with respect to the antenna orientations.

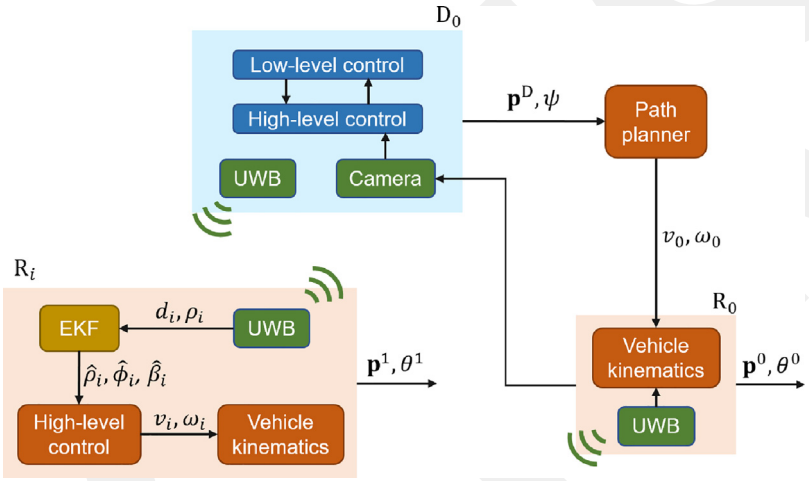

Fig. 7. The block diagram of the proposed framework.

R_0 and R_1 as in Fig. 6-left. In our framework, keeping the orientation of sensor s_0 constant, the angular variation of sensor s_1 corresponds to changing the angle ϕ_1. A sample dataset showing the variation of the measurement of the distance between the sensors and the true distance value acquired from our motion capture system is given in Fig. 6-right. It is observed that when $\phi_i \in [-\pi/3, \pi/3] \bigcup [-2\pi/3, 2\pi/3]$, the sensors yield distance measurements as characterized in the calibration results described in Section 4.2, while there might be fluctuations in the other regimes of ϕ_1. Therefore, we suggest calibrating the particular UWB sensors rigorously before implementing the proposed framework.

5. Real time relative localization

A robust localization algorithm for the entire system is designed under the sensing and communication constraints described in the previous section. Briefly, the drone tracks the leader UGV and acts as a moving UWB sensor whereas the follower UGVs utilize the inter-robot distances to estimate the relative positions to the leader UGV. This mutual relationship improves the localization performance and results in a coordinated team behavior.

A block diagram for the proposed framework is depicted in Fig. 7. Drone D_0 aims at tracking the leader UGV R_0 by utilizing its camera. The drone may be assigned a coleader role where it can guide the UGV R_0 to plan a path towards a possible goal location. The UWB sensors communicate wireless and generate the distances ρ_i, d_i, which are processed in the EKF localization algorithms of each follower UGV R_i, $i \in \{1, \dots, N\}$, separately. These estimations can be utilized in the high-level control layer of a UGV R_i, $i \in \{1, \dots, N\}$, for, e.g., building a formation. Remarkably, each follower UGV can utilize its own estimation in its high-level controller, which leads to a distributed framework.

5.1. Relative kinematics modeling

Assuming that all UGVs move on a Euclidean plane, the relative position system model between R_0 and R_i, $i \in \{1, \dots, N\}$, is derived in polar coordinates. Thus, the dynamics of the relative motion between the pair $\{\mathsf{R}_0, \mathsf{R}_i\}$, $i \in \{1, \dots, N\}$, is derived as follows:

$$\dot{\mathbf{x}}^i = \mathbf{f}(\mathbf{x}, \mathbf{u}) = \begin{bmatrix} -\mathbf{u}_1 \cos(\mathbf{x}_3) - \mathbf{u}_3 \cos(\mathbf{x}_2) \\ (1/\mathbf{x}_1)\left[\mathbf{u}_1 \sin(\mathbf{x}_3) + \mathbf{u}_3 \sin(\mathbf{x}_2)\right] + \mathbf{u}_4 \\ (1/\mathbf{x}_1)\left[\mathbf{u}_1 \sin(\mathbf{x}_3) + \mathbf{u}_3 \sin(\mathbf{x}_2)\right] + \mathbf{u}_2 \end{bmatrix}, \tag{10}$$

where $\mathbf{x}^i = [\rho_i, \phi_i, \beta_i]^\top$ is the state vector and $\mathbf{u} = [v_0, \omega_0, v_i, \omega_i]^\top$ is the input vector for the two-robot system $\{\mathsf{R}_0, \mathsf{R}_i\}$. Since the state consists of the relative variables only, this model does not depend on a coordinate frame. Thus, it is suitable for relative localization by onboard sensors without utilizing any infrastructure.

5.2. Drone motion control

Regarding the formation graph $\mathcal{G}(\mathcal{V}, \mathcal{E})$ of Section 3, the leader UGV R_0 moves with exogenous control commands based on a path

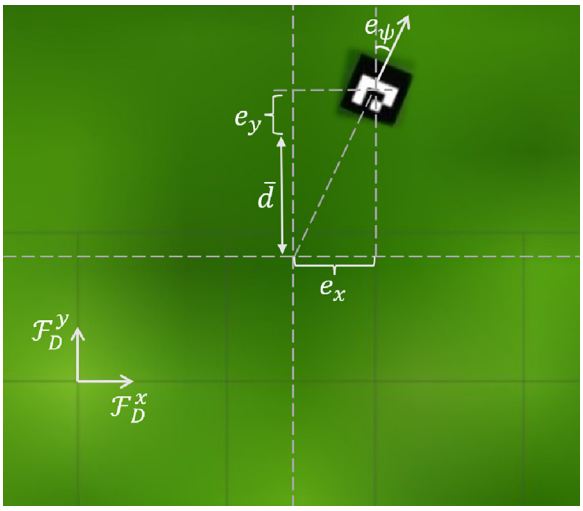

Fig. 8. The error variables e_x, e_y, e_ψ to be regulated by the drone as seen by the drone camera.

planning procedure. Drone D_0 is desired to track the leader R_0 from a certain distance to construct a triangle with the node set $\{\mathsf{R}_0, \mathsf{R}_i, \mathsf{D}_0\}$. Accordingly, drone D_0 equates its heading ψ to the heading of R_0 (θ_0) and maintains a certain distance $\bar{d}$ to R_0 in the positive y-axis of its body frame $\mathcal{F}_\mathrm{D}$ (Fig. 2). For this purpose, the leader R_0 is equipped with certain patterns overhead, e.g., Aruco pattern or quick response (QR) code, so that its relative heading angle can be acquired by the drone's camera. Thus, drone D_0 is commanded to fly at a suitable altitude $\bar{h}$ for a reliable pattern detection and applies the following control law on the horizontal plane:

$$\begin{aligned} \upsilon_D &= \left[k_{\mathrm{D}1} e_x, k_{\mathrm{D}2} e_y\right]^\top, \\ \omega_D &= k_{\mathrm{D}3} e_\psi, \end{aligned} \tag{11}$$

where e_x is the signed pixel error on the horizontal image plane, $e_y = \|\mathbf{p}_D - \mathbf{p}_0\| \cos(e_\psi) - \bar{d}$ is the distance error between D_0 and R_0, $e_\psi = \theta_0 - \psi$ is the heading error with respect to the UGV R_0, and $k_{\mathrm{D}1}, k_{\mathrm{D}2}, k_{\mathrm{D}3}$ are positive control gains (Fig. 8). That is, drone D_0 aims at regulating its heading and position in the x-axis of its body frame $\mathcal{F}_\mathrm{D}$ while maintaining the desired distance $\bar{d}$ toward the leader R_0. In Section 8, a suitable margin for $\bar{d}$ is suggested, and the effect of $\bar{d}$ on the system performance is analyzed. Notably, since a proportional control law is applied, it is not necessary to use the actual distance (e_x) and angle (e_ψ) error values for regulation. Thus, these errors are calculated in pixel values from the image.

5.3. Observability analysis and estimator design

With the drone D_0 controlled to move in the above configuration, the following relation can be obtained:

$$\beta_i = \pi + \mathrm{s}(\mathsf{R}_i)\alpha_{0i}, \tag{12}$$

$$\alpha_{0i} = \arccos\left(\frac{\rho_i^2 + \bar{d}^2 - d_i^2}{2\rho_i \bar{d}}\right) \tag{13}$$

where $\mathrm{s}(\mathsf{R}_i) = 1$ for $\mathsf{R}_i \in \mathcal{S}_L$ and $\mathrm{s}(\mathsf{R}_i) = -1$ for $\mathsf{R}_i \in \mathcal{S}_R$ (Fig. 2), and α_{0i} is the internal angle of the triangle $\{\mathsf{R}_i, \mathsf{R}_0, \mathsf{D}_0\}$.

Each follower UGV R_i, $i \in \{1, \dots, N\}$, measures the distance ρ_i utilizing the onboard UWB sensors. Also, by acquiring the drone-leader UGV distances d_i, each follower UGV measures its bearing angle β_i through the relation (12). However, since the UGVs are not equipped with a compass sensor, their relative heading angles ϕ_i are not measured directly. Therefore, the measurement model for R_i is given by:

$$\mathbf{y}^i = \left[\rho_i, \beta_i\right]^\top. \tag{14}$$

In the proposed framework, the heading angles θ_i, $i \in \{0, \dots, N\}$, and ψ with respect to the fixed frame $\mathcal{F}_\mathrm{G}$ are not measured or estimated. Commonly, the heading angles are required for executing a global mission for the HMRS such as reaching a target region which is beyond the line-of-sight of the robots. Remarkably, this work focuses on the design of a relative localization algorithm that can generate the relative position estimates within the team. If desired, any global path planning objective can be implemented by equipping the leader robot R_0 with global sensors, which would not affect the proposed framework.

The following result summarizes the conditions for the observability of the state vector $\mathbf{x}_i$ regarding the dynamics (10) and the measurement model (14).

Proposition 5.1. *Consider the HMRS $\mathcal{M}$ comprised of the UGVs R_i, $i \in \{0, \dots, N\}$, with the motion model (1), (2), the drone D_0, and the underlying formation graph $\mathcal{G}(\mathcal{V}, \mathcal{E})$. Under the sensing and communication assumptions given thus far, the state $\mathbf{x}^i$ is locally weakly observable if $|\upsilon_i(t)| > 0$, $i \in \{1, \dots, N\}$.*

Proof. First, a brief background about the observability of nonlinear systems is given based on the analysis of Hermann and Krener (1977) which provides a systematic way to examine the observability of nonlinear systems. Consider the system

$$\dot{\mathbf{x}} = \mathbf{f}(\mathbf{x}, \mathbf{u}), \quad \mathbf{y} = \mathbf{h}(\mathbf{x}), \tag{15}$$

where $\mathbf{x} \in \mathfrak{R}^n, \mathbf{u} \in \mathfrak{R}^m, \mathbf{y} \in \mathfrak{R}^n$, and $\mathbf{f}, \mathbf{h}$ are smooth (infinitely differentiable) functions. Define the gradient $\mathrm{d}(\cdot) = \left[\frac{\partial}{\partial x_1}, \dots, \frac{\partial}{\partial x_n}\right]$ as a row vector valued function, where $\frac{\partial}{\partial x_i}$ denotes the partial derivative with respect to x_i. Denote the observability matrix for the system (15) by

$$\mathcal{O} = \left[(\mathrm{d}(\mathcal{L}_\mathbf{f}^0\mathbf{h}))^\top, (\mathrm{d}(\mathcal{L}_\mathbf{f}^1\mathbf{h}))^\top, \cdots, (\mathrm{d}(\mathcal{L}_\mathbf{f}^i\mathbf{h}))^\top\right]^\top, \tag{16}$$

where $\mathcal{L}$ denotes the Lie derivative, i.e., $\mathcal{L}_\mathbf{f}^0\mathbf{h} = \mathbf{h}$, $\mathcal{L}_\mathbf{f}^1\mathbf{h} = \mathrm{d}(\mathcal{L}_\mathbf{f}^0\mathbf{h})\mathbf{f}$, and $\mathcal{L}_\mathbf{f}^i\mathbf{h} = \mathrm{d}(\mathcal{L}_\mathbf{f}^{i-1}\mathbf{h})\mathbf{f}$, for $i \in \mathbb{N}$. Notably, the first entry of the matrix $\mathcal{O}$ is the Jacobian of $\mathbf{h}$. The system (15) is called *locally weakly observable* if $\mathcal{O}$ is full rank. Another interpretation of the locally weakly observability is that the state $\mathbf{x}$ can be distinguished from its neighbors for every admissible inputs for some time interval $[t_0, t_1]$ (Hermann & Krener, 1977).

Next, the observability matrix for the system (10)–(14) for a follower robot R_i is derived. The first block of $\mathcal{O}$ is given by:

$$\mathrm{d}(\mathcal{L}_\mathbf{f}^0\mathbf{h}) = \mathrm{d}(\mathbf{h}) = \begin{bmatrix} 1 & 0 & 0 \\ 0 & 0 & 1 \end{bmatrix}. \tag{17}$$

Since $\mathrm{d}(\mathbf{h})$ does not satisfy the rank condition, i.e., $\mathrm{rank}(\mathrm{d}(\mathbf{h})) = 2 < 3$, one needs to continue evaluating the next two rows of the matrix $\mathcal{O}$ as follows:

$$\begin{aligned} \mathrm{d}(\mathcal{L}_\mathbf{f}^1\mathbf{h}) &= \mathrm{d}(\mathrm{d}(\mathcal{L}_\mathbf{f}^0\mathbf{h})\mathbf{f}) \\ &= \mathrm{d}\left(\begin{bmatrix} -\mathbf{u}_1 \cos(\mathbf{x}_3) - \mathbf{u}_3 \cos(\mathbf{x}_2) \\ (1/\mathbf{x}_1)\left[\mathbf{u}_1 \sin(\mathbf{x}_3) + \mathbf{u}_3 \sin(\mathbf{x}_2)\right] + \mathbf{u}_2 \end{bmatrix}\right) \\ &= \begin{bmatrix} 0 & \mathbf{u}_3 \sin(\mathbf{x}_2) & \mathbf{u}_1 \sin(\mathbf{x}_3) \\ m_{21} & (\frac{1}{\mathbf{x}_1})\mathbf{u}_3 \cos(\mathbf{x}_2) & (\frac{1}{\mathbf{x}_1})\mathbf{u}_1 \cos(\mathbf{x}_3) \end{bmatrix}, \end{aligned}$$

where

$$m_{21} = -\frac{1}{\mathbf{x}_1^2}\left[\mathbf{u}_1 \sin(\mathbf{x}_3) + \mathbf{u}_3 \sin(\mathbf{x}_2)\right].$$

It then follows that

$$\mathcal{O} = \begin{bmatrix} 1 & 0 & 0 \\ 0 & 0 & 1 \\ 0 & \mathbf{u}_3 \sin(\mathbf{x}_2) & \mathbf{u}_1 \sin(\mathbf{x}_3) \\ m_{21} & (\frac{1}{\mathbf{x}_1})\mathbf{u}_3 \cos(\mathbf{x}_2) & (\frac{1}{\mathbf{x}_1})\mathbf{u}_1 \cos(\mathbf{x}_3) \\ & \vdots & \end{bmatrix}. \tag{18}$$

Due to the physical properties of the robots, it holds that $\mathbf{x}_1(t) = \rho(t) > \rho_{\min} > 0$. Also, the velocity inputs are bounded by the assumption in Section 3. Thus, the matrix entries are bounded. It is clear that the rank condition of $\mathcal{O}$ is determined by the entries $\mathbf{u}_3 \sin(\mathbf{x}_2)$ and $(\frac{1}{\mathbf{x}_1})\mathbf{u}_3 \cos(\mathbf{x}_2)$, i.e., $\mathcal{O}$ in (18) is rank deficient if both of these terms are zero, which can occur only when $\mathbf{u}_3 = v_i = 0$. Therefore, if $v_i(t) > 0$, $i \in \{1, \dots, N\}$ for all t, then $\mathcal{O}$ is full rank, and the state $\mathbf{x}^i$ is locally weakly observable. □

Essentially, Proposition 5.1 implies that the entire state vector $\mathbf{x}^i$ can be estimated as long as all UGVs have nonzero linear velocities, which can be satisfied with a suitable formation controller design. Furthermore, the locally weakly observability of the state can be interpreted as each follower UGV R_i, $i \in \{1, \dots, N\}$, can estimate the unmeasured state $\mathbf{x}_2 = \phi_i$ during an operation. In light of this result, a discrete-time observer for each follower UGV R_i, $i \in (1, \dots, N)$ is designed in the following.

If the first-order linearization of a model sufficiently approaches to the original model and if the actuator and sensor noises can be approximated by Gaussian distributions, then an extended Kalman filter (EKF) produces a sufficient performance. In fact, in most cases, EKF provides an almost optimal performance for state estimation for nonlinear kinematics/dynamics which do not include extreme nonlinearities. In the present case, the relative pose model (10) derived for two UGVs is infinitely differentiable and do not contain switching terms. Also, considering the practical indoor application scenarios, the UGV speeds are usually maintained bounded in formation tasks (e.g., less than 0.2 in both linear and angular speeds). Therefore, the first-order approximation is expected to yield satisfactory performance in state estimation. Moreover, the simple and easy-to-apply iterative algorithm of EKF can run on an average microcontroller (e.g., a Raspberry Pi board). Therefore, EKF remains a viable and suitable estimation method to be used onboard of the UGVs.

Accordingly, an EKF is designed to track the states on each follower UGV R_i, $i \in (1, \dots, N)$. A comparison of EKF with a particle filter is given in Section 9. A pseudocode for the estimation algorithm on robot R_i is given in Algorithm 1, where

$$\mathbf{G} = \mathbf{I}_3 + \begin{bmatrix} 0 & \mathbf{u}_3 \sin(\mathbf{x}_2) & \mathbf{u}_1 \sin(\mathbf{x}_3) \\ g_{21} & (1/\mathbf{x}_1)\mathbf{u}_3 \cos(\mathbf{x}_2) & (1/\mathbf{x}_1)\mathbf{u}_1 \cos(\mathbf{x}_3) \\ g_{21} & (1/\mathbf{x}_1)\mathbf{u}_3 \cos(\mathbf{x}_2) & (1/\mathbf{x}_1)\mathbf{u}_1 \cos(\mathbf{x}_3) \end{bmatrix} T_s,$$

$$g_{21} = \left(\frac{-1}{\mathbf{x}_1^2}\right)\left[\mathbf{u}_1 \sin(\mathbf{x}_3) + \mathbf{u}_3 \sin(\mathbf{x}_2)\right], \quad \mathbf{H} = \begin{bmatrix} 1 & 0 & 0 \\ 0 & 0 & 1 \end{bmatrix},$$

with T_s the sampling time. Therefore, Algorithm 1 generates iteratively the estimates $\hat{\rho}_i, \hat{\phi}_i, \hat{\beta}_i$ for the state variables ρ_i, ϕ_i, β_i on each UGV R_i, $i \in (1, \dots, N)$.

In the proposed system, each UGV R_i estimates its relative position to R_0 independently. In this sense, the proposed framework differs from collaborative localization in which all team members update the same state vector estimate in a centralized manner which may require a high bandwidth communication environment. Here, each UGV R_i, $i \in (1, \dots, N)$ needs to obtain the velocities v_0, ω_0 of the leader R_0, which can be satisfied with the communication medium the onboard UWB sensors generate.

6. Distributed formation control algorithm design

In this section, the applicability of the proposed relative localization framework is demonstrated on two customly designed formation control algorithms. Notably, since the localization framework is decentralized, i.e., each follower UGV R_i, $i \in \{1, \dots, N\}$, estimates the relative configuration between itself and the leader R_0, a formation control algorithm can be implemented together with the proposed localization framework in a distributed manner. The formation control algorithms are presented in the following.

Algorithm 1 EKF for robot R_i

Require: $\hat{\mathbf{x}}[k-1], \mathbf{S}[k-1], \mathbf{u}[k], \mathbf{Q}, \mathbf{R}$

Ensure: $\hat{\mathbf{x}}[k], \mathbf{S}[k]$

$\mathbf{G}[k] \leftarrow \frac{f(\partial \mathbf{x}, \mathbf{u})}{\partial \mathbf{x}}|_{\mathbf{x}=\hat{\mathbf{x}}[k-1]}$

$\mu[k] \leftarrow f(\hat{\mathbf{x}}[k-1], \mathbf{u}[k])$ ▷ Prediction

$\mathbf{S}[k] \leftarrow \mathbf{G}[k]\mathbf{S}[k-1]\mathbf{G}[k]^T + \mathbf{R}$

$\mathbf{y}[k] \leftarrow \left[\rho_i[k], \beta_i[k]\right]^\top$

$\mathbf{K}[k] \leftarrow \mathbf{S}[k]\mathbf{H}^T(\mathbf{H}\mathbf{S}[k]\mathbf{H}^T + \mathbf{Q})^{-1}$

$\hat{\mathbf{x}}[k] \leftarrow \mu[k] + \mathbf{K}[k](\mathbf{y}[k] - \mathbf{h}(\mu[k]))$ ▷ Update

$\mathbf{S}[k] \leftarrow (I - \mathbf{K}[k]\mathbf{H})\mathbf{S}[k]$

6.1. Formation acquisition control

First, we focus on the formation acquisition problem which is defined as follows:

Objective 2. *Consider the HMRS with the UGV team R_i, $i \in \{0, \dots, N\}$, and drone D_0 with the properties defined in Section 3. Assuming that $v_0 = \omega_0 = 0$ and that the drone is configured as in Section 5.2, derive the control signals required to steer the follower UGVs R_i, $i \in \{1, \dots, N\}$, toward their desired configurations $\{\rho_i^{\text{des}}, \beta_i^{\text{des}}\}$ by satisfying the velocity constraint imposed by Proposition 5.1.*

To solve Objective 2, first a fictitious controller is derived, and a convergence analysis is provided, with the assumption that the actual values of the variables ρ_i, ϕ_i, β_i are available to a follower robot R_i. Then, the actual variables are replaced by their estimated values in the controller, and the controller's performance is observed. Notably, this two-step process is common in the estimation-based control literature (Ioannou & Fidan, 2006).

When drone D_0 hovers at its desired location behind the leader UGV R_0, the system configuration can be depicted as in Fig. 9. Here, a follower UGV R_i, $i \in \{1, \dots, N\}$, aims at converging to its desired location $\mathbf{p}_i^{\text{des}}$ where $\rho_i = \rho_i^{\text{des}}, \beta_i = \beta_i^{\text{des}}$. Let $e_\rho = \rho_i^{\text{des}} - \rho_i$, $e_\beta = \beta_i^{\text{des}} - \beta_i$ denote the error variables where ρ_i^{des}, β_i^{des} are respectively the desired distance and bearing angle of a follower UGV R_i, $i \in \{1, \dots, N\}$. Also, observe that

$$\gamma_i = \arccos\left(\frac{\rho_i^2 + \delta_i^2 - \left(\rho_i^{\text{des}}\right)^2}{2\rho_i\delta_i}\right), \tag{19}$$

$$\delta_i = \sqrt{\rho_i^2 + \left(\rho_i^{\text{des}}\right)^2 - 2\rho_i\rho_i^{\text{des}}\cos(|e_\beta|)}. \tag{20}$$

The following adaptive controller for UGV R_i, $i \in \{1, \dots, N\}$ is proposed:

$$v_i = \begin{cases} \bar{v}_i, & \text{if } |e_\rho| > \rho_{\text{th}}, \\ 0, & \text{otherwise.} \end{cases} \tag{21}$$

$$\omega_i = \begin{cases} -k_\omega(t)\text{sgn}(\eta_i(t)), & \text{if } |e_\rho| > \rho_{\text{th}}, \\ 0, & \text{otherwise,} \end{cases} \tag{22}$$

where $k_\omega(t) > \frac{\bar{v}_i}{\delta_i(t)} > 0$ is the adaptive controller gain, $\rho_{\text{th}} > 0$ is a design constant defining the desired disk $\mathcal{B}(\mathbf{p}_i^{\text{des}}, \rho_{\text{th}})$ for a UGV R_i, and $\text{sgn}(\cdot)$ is the signum function. In essence, the controller (21), (22) aims at driving the follower UGV R_i towards the desired location $\mathbf{p}_i^{\text{des}}$ until R_i enters the disk $\mathcal{B}(\mathbf{p}_i^{\text{des}}, \rho_{\text{th}})$, i.e., $|e_\rho| \leq \rho_{\text{th}}$. The convergence properties of the proposed controller is given in the following proposition.

Proposition 6.1. *Consider Objective 2 for a follower UGV R_i, $i \in \{1, \dots, N\}$. Assume that initially $\rho_i(0) > \rho_i^{\text{des}} + \rho_{\text{th}}$ and $-\frac{\pi}{2} + \epsilon < \eta_i(0) < \frac{\pi}{2} - \epsilon$ for an arbitrarily small $\epsilon > 0$. If the controller (21), (22) is applied, then the UGV R_i converges to the disk $\mathcal{B}(\mathbf{p}_i^{\text{des}}, \rho_{\text{th}})$ asymptotically.*

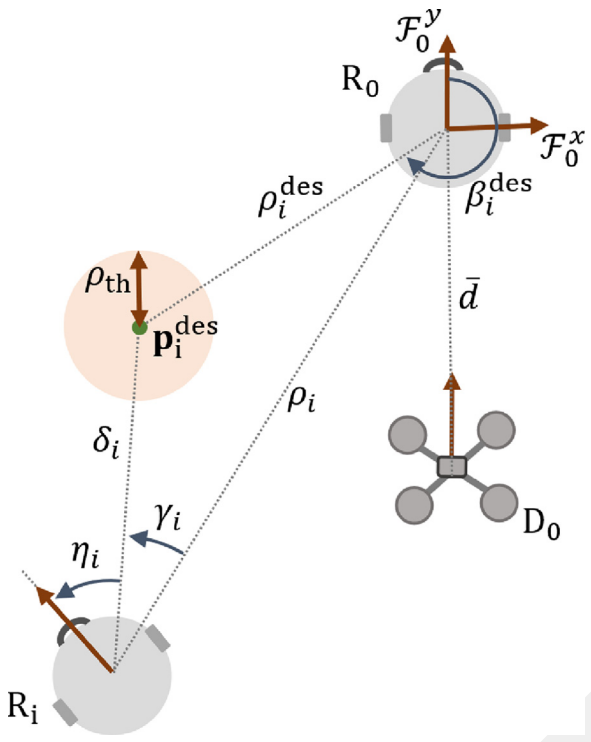

Fig. 9. The desired configuration of UGV R_i in the formation acquisition case. The desired disk $\mathcal{B}(\mathbf{p}_i^{des}, \rho_{th})$ is depicted with the orange color. (For interpretation of the references to color in this figure legend, the reader is referred to the web version of this article.)

Proof. Since $v_0(t) = \omega_0(t) = 0$ for all $t > 0$, the relative motion dynamics between the center of the UGV R_i and its desired position $\mathbf{p}_i^{des}$ reads

$$\dot{\delta}_i = -\bar{v}_i \cos(\eta_i) \tag{23}$$

$$\dot{\eta}_i = \frac{1}{\delta_i} \bar{v}_i \sin(\eta_i) + \omega_i, \tag{24}$$

where δ_i, η_i define the new polar dynamics (Fig. 9). For the region $\rho_i(t) > \rho_{th}$, define $V = \frac{1}{2}\eta_i^2(t)$ as the Lyapunov function. It then follows that

$$\dot{V}(t) = \eta_i(t) \left[\frac{\bar{v}_i}{\delta_i(t)} \sin(\eta_i(t)) - k_\omega(t) \text{sgn}(\eta_i(t)) \right] \tag{25}$$

$$= -k_\omega(t) \left| \eta_i(t) \right| + \frac{\bar{v}_i}{\delta_i(t)} \sin(\eta_i)\eta_i(t) \tag{26}$$

$$\leq \left(-k_\omega(t) + \frac{\bar{v}_i}{\delta_i(t)} \right) \left| \eta_i(t) \right|. \tag{27}$$

Since by definition $k_\omega(t) > \frac{\bar{v}_i}{\delta_i(t)} > 0$ in the considered region, we have that $\dot{V}(t) \leq 0$ for all t. Then, from the LaSalle's invariance principle, it follows that $\eta_i(t)$ converges to zero as $t \to \infty$ (Khalil, 2001). It is clear from (23) that if $-\frac{\pi}{2} < \eta_i(t) < \frac{\pi}{2}$, then $\dot{\delta}_i(t) < 0$. Then, there exists a time instant $t_\rho > 0$ such that $\delta_i(t_\rho) \leq \rho_{th}$ for an arbitrarily small ρ_{th}, which concludes the proof. □

Proposition 6.1 establishes that if the actual values of ρ_i, ϕ_i, β_i are used, then the proposed control law (21), (22) steers a follower UGV R_i inside the disk $\mathcal{B}(\mathbf{p}_i^{des}, \rho_{th})$. Next, the estimation outputs $\hat{\rho}_i, \hat{\phi}_i, \hat{\beta}_i$ generated by the EKF are used in place of their actual values in the control law (21), (22). For a reliable estimation process, the initial and desired values of the inter-UGV angles $\beta_i(0), \beta_i^{des}$ need to satisfy the constraint given in Assumption 3.1. Particularly, the follower UGVs must be initiated not too close to the line l_{0D} by choosing a suitable threshold β_{th}. In Sections 7 and 8, the simulation and experimental results of the proposed estimation-control framework are provided.

6.2. Formation maintaining control

Consider the following formation maintaining problem:

Objective 3. *Consider the HMRS with the UGV team* R_i, $i \in \{0, \dots, N\}$, *and drone* D_0 *with the properties defined in Section 3. Assume that the leader UGV* R_0 *moves with nonzero linear velocity* v_0 *by obeying the constraint (4) and that the drone tracks* R_0 *as described in Section 5.2. Derive the control signals required to steer the follower UGVs* R_i, $i \in \{1, \dots, N\}$, *so that they maintain a given desired configuration* $\{\rho_i^{des}, \beta_i^{des}\}$ *by satisfying the velocity constraint imposed by Proposition 5.1.*

The majority of the previous formation maintaining control schemes require the knowledge of the robots' heading angles with respect to a fixed frame and thus require magnetometer measurements, which may not be practical for the reasons explained in Section 1. Therefore, an ad hoc practical formation control algorithm is proposed here with two properties: It does not rely on a magnetometer measurement and it satisfies the nonzero linear velocity constraint imposed by Proposition 5.1. A follower UGV R_i, $i \in \{1, \dots, N\}$, aims to estimate the distance ρ_i and relative angles ϕ_i, β_i and maintain the variables ρ_i, β_i at their desired values $\rho_i^{des}, \beta_i^{des}$. Note that if ρ_i, β_i are maintained at their desired values, the formation induced by the graph $\mathcal{G}(\mathcal{V}, \mathcal{E})$ will be preserved in the leader UGV's body frame $\mathcal{F}_0$. Let $e_\rho = \rho_i - \rho_i^{des}$, $e_\beta = \beta_i - \beta_i^{des}$ denote the error variables where ρ_i^{des}, β_i^{des} are respectively the desired distance and bearing angle of a follower UGV R_i, $i \in \{1, \dots, N\}$. Therefore, the main goal for the formation control algorithm is to maintain the errors e_ρ, e_β bounded. Since the UGVs cannot sense their heading angles due to the lack of magnetometer sensors onboard, the heading angles are not controlled to track a certain reference value.

The following fictitious switching controller is proposed for a follower UGV R_i, $i \in \{1, \dots, N\}$:

$$[v_i, \omega_i] = \begin{cases} [-0.5v_0, \ -k_\omega e_\phi], & \text{if in Region 1} \\ [-0.5v_0, \ -k_\omega \phi_i], & \text{if in Region 2} \\ [v_0, \ -k_\omega e_\beta], & \text{if in Region 3} \\ [2v_0, \ -k_\omega \phi_i], & \text{if in Region 4} \\ [v_0, \ \bar{\omega}], & \text{if in Region 5} \end{cases} \tag{28}$$

where $e_\phi = \phi_i - (\beta_i^{des} - \pi)$ is the relative bearing error, $k_\omega > 0$ is the control gain, and the regions are defined as follows:

- Region 1: $\frac{3\pi}{2} - \beta^{th} < \beta_i(t) < \beta_i^{des} + \bar{\beta}$,
- Region 2: $\beta_i^{des} - \bar{\beta} \leq \beta_i(t) \leq \beta_i^{des} + \bar{\beta}$ and $\rho_i(t) < \rho^{des} - \bar{\rho}$,
- Region 3: $\beta_i^{des} - \bar{\beta} \leq \beta_i(t) \leq \beta_i^{des} + \bar{\beta}$ and $\rho^{des} - \bar{\rho} \leq \rho_i(t) \leq \rho^{des} + \bar{\rho}$,
- Region 4: $\beta_i^{des} - \bar{\beta} \leq \beta_i(t) \leq \beta_i^{des} + \bar{\beta}$ and $\rho_i(t) > \rho^{des} + \bar{\rho}$,
- Region 5: $\beta_i^{des} + \bar{\beta} < \beta_i(t) < \pi + \beta^{th}$.

Here, the design constants $\bar{\rho}, \bar{\beta}$ are used to define the desired region for the UGV R_i in which the distance and bearing errors e_ρ, e_β are maintained bounded. The constant β^{th} is used to keep the follower UGV away from the line l_{0D} to avoid collinear robots case (refer to Assumption 3.1). These constants can be chosen same for all follower UGVs R_i. As in the formation acquisition case, we propose to use the estimation outputs $\hat{\rho}_i, \hat{\phi}_i, \hat{\beta}_i$ generated by the EKF in place of their actual values in the control law (28). The experimental results with this controller are demonstrated in Section 8.

7. Simulations

A Gazebo environment was built with ROS interface, including five Rosbot UGVs placed in a hexagon formation with the leader (R_0) in the front and an Iris drone (Fig. 1(a)). An Aruco pattern was mounted on the leader Rosbot to be able to detect its heading angle by a mono camera attached at the bottom of the drone. Each follower UGV performed relative position estimation independently obeying the state

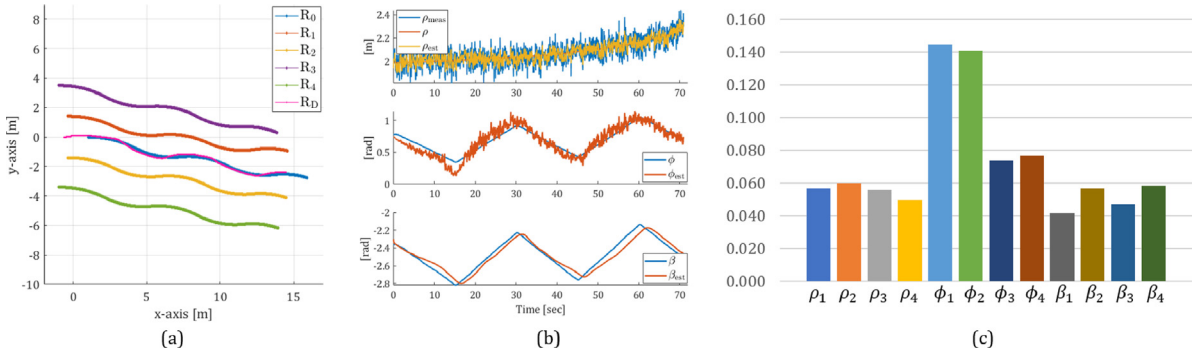

Fig. 10. Simulation results: (a) traces of the robots in an s-path simulation; (b) estimations; (c) Averages of the RMSE $\mathrm{E}^i_\rho, \mathrm{E}^i_\phi, \mathrm{E}^i_\beta$ in 10 experiments.

and observation models given in Section 5. The drone was equipped with a px4 flight control software which handled the low-level control and received the high-level planar velocity and yaw rate commands. All robots ran their estimation code at 20 Hz. The UWB distance measurements between the UGVs were simulated by adding a zero mean Gaussian noise on the distance values acquired from Gazebo.

7.1. Exogenous inputs

First, the localization algorithm performance for UGVs commanded with exogenous velocities was evaluated. Fig. 10-(a) shows the traces of the robots and the estimation results of a simulation. In this simulation, the UGVs were initiated from the following positions: $\mathbf{p}_0(0) = [1,0]^\top$, $\mathbf{p}_1(0) = [-0.5,1.5]^\top$, $\mathbf{p}_2(0) = [-0.5,-1.5]^\top$, $\mathbf{p}_3(0) = [-1,3.5]^\top$, $\mathbf{p}_4(0) = [-1,-3.5]^\top$, $\mathbf{p}^D(0) = [-0.5,0]^\top$ m with the heading angles $\theta_i(0) = 0$ rad. Notably, this initial condition was chosen to reflect a formation scenario. All UGVs moved on an s-shaped path with constant linear velocities and periodic angular velocities, and the drone D_0 followed R_0 using the control algorithms given in Section 5. It was observed that the estimations $\hat{\rho}_i, \hat{\phi}_i, \hat{\beta}_i$ tracked their actual values $\rho_i(t), \phi_i(t), \beta_i(t)$ with an acceptable error margin. Remarkably, although the state ϕ_i was not measured directly, the estimation error for ϕ_i remained small since it was an observable state (Fig. 10-(b)).

Next, define the estimation root-mean-square errors (RMSE) for the inter-robot distances and the relative heading angles in an experiment by

$$\mathrm{E}^i_\rho = \left(\frac{1}{K}\sum_{k=1}^{K}\left(\hat{\rho}_i[k]-\rho_i[k]\right)^2\right)^{\frac{1}{2}},\quad \mathrm{E}^i_\phi = \left(\frac{1}{K}\sum_{k=1}^{K}\left(\hat{\phi}_i[k]-\phi_i[k]\right)^2\right)^{\frac{1}{2}},$$

$$\mathrm{E}^i_\beta = \left(\frac{1}{K}\sum_{k=1}^{K}\left(\hat{\beta}_i[k]-\beta_i[k]\right)^2\right)^{\frac{1}{2}},$$

where K is the total time steps during an experiment and $i = \{1,2,3,4\}$ is the follower UGV index. Fig. 10-(c) shows the estimation RMSE of 10 simulations conducted with the same configuration as Fig. 1(a). In these simulations, the UGVs were driven with several velocity commands resulting in a variety of paths such as lines, arcs, and s-paths. It was observed that while $\mathrm{E}_\rho, \mathrm{E}_\beta$ which correspond to the measured variables remained below 0.1 m and 0.1 rad, respectively, E_ϕ could reach 0.14 rad (which corresponds to the unmeasured state). Remarkably, these RMSE values can be considered sufficiently good for a distance-only estimation mechanism, especially when compared to Güler et al. (2019, 2018), Wang et al. (2017).

7.2. Formation acquisition

In the second simulation study, the performance of the estimation-control framework proposed in Section 6.1 was evaluated on the same robotic setup. In this case, the follower UGVs R_i, $i = \{1,2,3,4\}$ aimed at reaching their desired positions around the leader UGV R_0 by applying

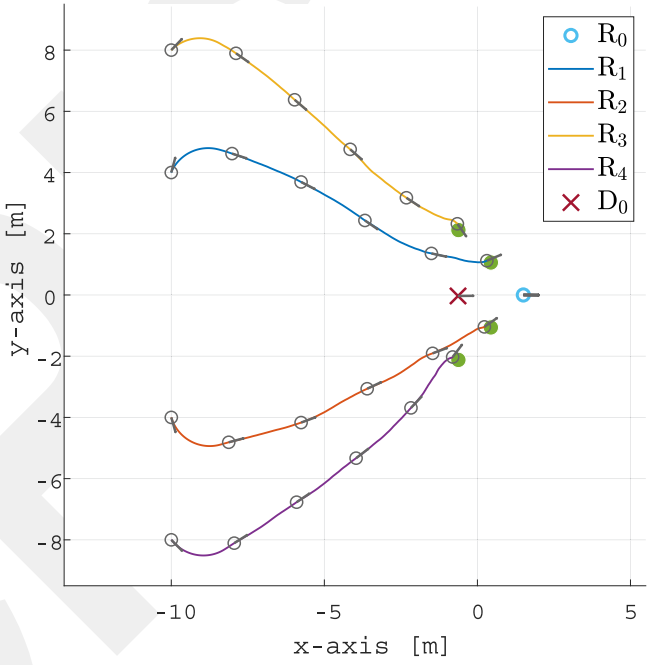

Fig. 11. The traces of the four follower UGVs in a formation acquisition simulation (D_0: red cross, R_0: blue circle, R_i, $i = \{1,2,3,4\}$: gray circles; the headings of the robots are shown with gray arrows). The UGVs start from their initial locations with random heading angles and aim at reaching their desired regions indicated by the green colored disks, by utilizing only the UWB distances without measuring their heading angles.

the control law (21), (22) independently of each other. In accordance with Sections 4 and 5, each UGV R_i was assumed to obtain the distances ρ_i, d_i corrupted with additive zero-mean Gaussian noise with standard deviation of $\sigma_d = 0.025$ m. Accordingly, β_i was constructed through (12). We note that the heading angles θ_i and the bearing angles ϕ_i are not measured. Thus, the control law used the estimation $\hat{\phi}_i$ to calculate the error term η_i in (22).

To verify the efficiency, the follower UGVs were initiated from varying configurations at large distances away from their desired locations (up to 10 m). In all simulations, the following values were used: $\bar{v}_i = 0.3$ m/s, $\rho_{\mathrm{th}} = 0.25$ m, and $k_\omega(t) = \frac{\bar{v}_i}{\delta_i(t)} + 0.2$. The traces of the UGVs in a simulation are depicted in Fig. 11. Although the UGVs started their motion with randomly chosen initial heading values, they reached the disks $\mathcal{B}(\mathbf{p}_i^{\mathrm{des}}, \rho_{\mathrm{th}})$ around their desired locations $\mathbf{p}_i^{\mathrm{des}}$ (depicted with the green colored disks). The error variables $\delta_i, \eta_i, e_\beta$ are presented in Fig. 12. It can be observed that while $\delta_i(t)$ monotonically converge to zero, the orientation errors e_β remain bounded and converge to a neighborhood of zero. Remarkably, although η_i plays a key role in the control rule (22), it does not carry meaning for the formation

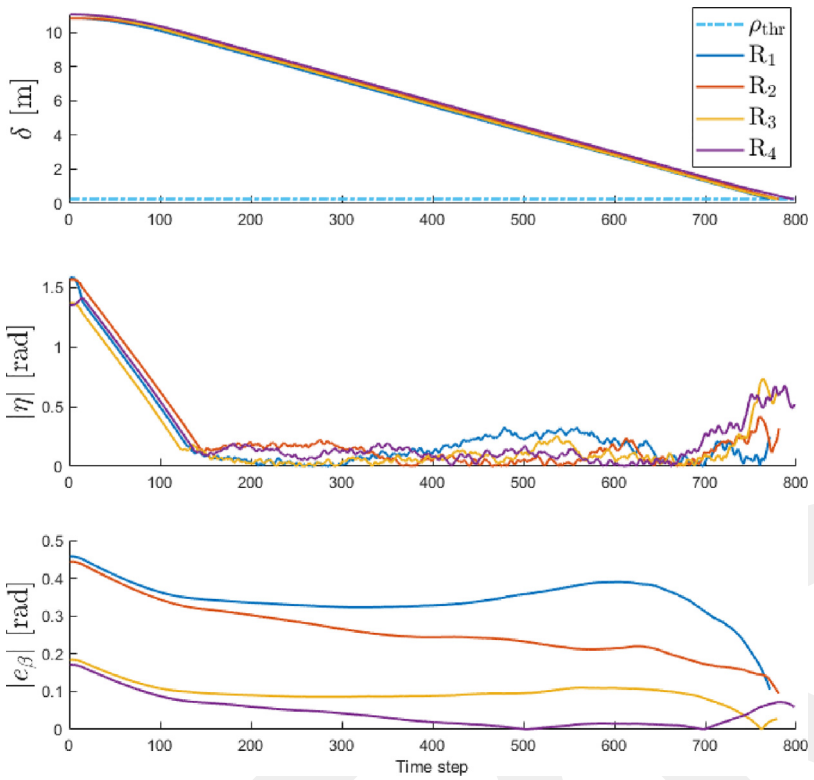

Fig. 12. The error variables in an estimation-based formation acquisition control simulation.

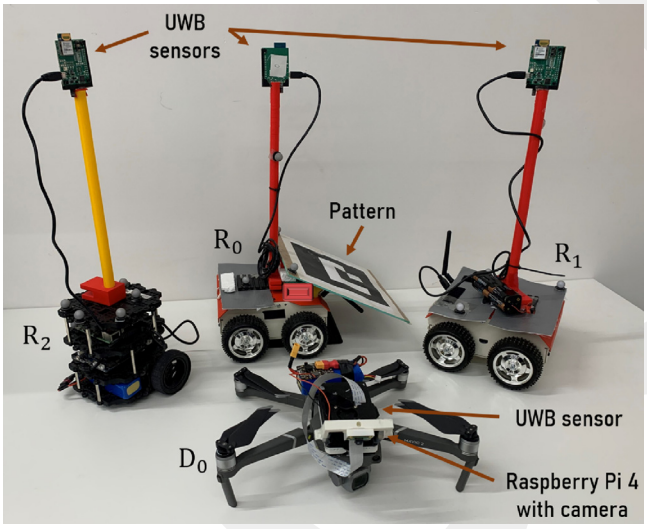

Fig. 13. The robotic system used in the experiments.

acquisition task alone: It is used to steer a follower UGV toward its desired location based on the estimation $\hat{\phi}_i$. In other words, once a follower UGV enters its desired disk, the formation acquisition task is achieved.

8. Experiments

To evaluate the proposed system's effectiveness in practice, several experiments were conducted on real robots. The experimental setup consisted of a DJI Mavic 2 drone and three non-holonomic UGVs (two Rosbots and a Turtlebot) (Fig. 13). A Rosbot was assigned as the leader (R_0), and the other UGVs ran their estimation algorithms to estimate the relative variables $\rho_i, \phi_i, \beta_i, i \in (1, 2)$. Each UGV was equipped with calibrated Decawave MDEK1001 UWB distance sensors at their centers with a ground clearance of 0.5 meters to minimize the multi-path effects. The drone was equipped with a Raspberry Pi4 board and a monocular camera for the leader UGV detection and high-level computations. The high-level motion commands, i.e., the planar velocities on the x–y plane and yaw rate commands, are sent to the remote controller of the drone through a mobile phone running the mobile support development kit (MSDK), all of which operated in the autonomous mode without human interruption except take-off and landing. The ground truth position data were collected with a Vicon motion capture system installed in a 5x6 meters flight zone. The mocap data was not utilized in any part of the framework. The drone could detect the Aruco pattern reliably at the altitude range $h \in [1, 2.2]$ meters. The altitude was set to $\bar{h} = 1.5$ m for a safe flight in the indoor lab environment. The drone's high-level controller given in Section 5.2 was tuned to follow smoothly the leader UGV's pattern. Particularly, the following parameter values were used: $k_{\text{D1}} = 0.05$, $k_{\text{D2}} = 1.1$, $k_{\text{D3}} = 1$. Remarkably, tuning of these gains depends on several factors such as the drone dynamics, wind conditions, experiment environment, battery level, the accuracy of the low-level controller, and camera detection rates. Therefore, tuning of these parameters before an operation is suggested for smooth tracking of the leader robot R_0.

8.1. Exogenous inputs

In the first set of experiments, the goal was to demonstrate the estimation capability of the framework without considering the formation maintaining task. Thus, all UGVs were steered with exogenous velocity commands. An experiment's result is given in Fig. 14 where the UGVs followed an s-shaped path with constant linear velocities $v_i = 0.08$ m/s and periodic angular velocities $\omega_i = \pm 0.05$ rad/s (Fig. 14-left). The estimated variables together with their ground truth values obtained from the mocap system are presented in Fig. 14-right. It was observed that the UGVs R_1, R_2 estimated the variables $\hat{\rho}_i, \hat{\phi}_i, \hat{\beta}_i$ with low

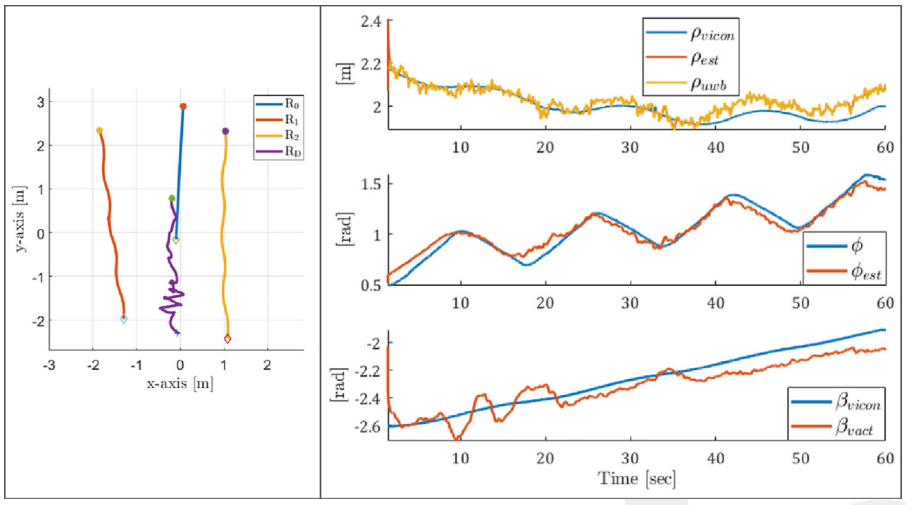

Fig. 14. Results of an experiment with exogenous control inputs: (Left) Traces of the robots; (Right) estimates of the variables $\hat{\rho}_1, \hat{\phi}_1, \hat{\beta}_1$ in UGV R_1.

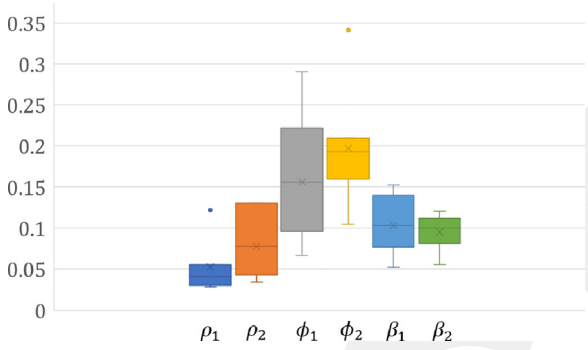

Fig. 15. RMSE of the relative position estimations in six experiments: ρ_i in meters; ϕ_i, β_i in radians.

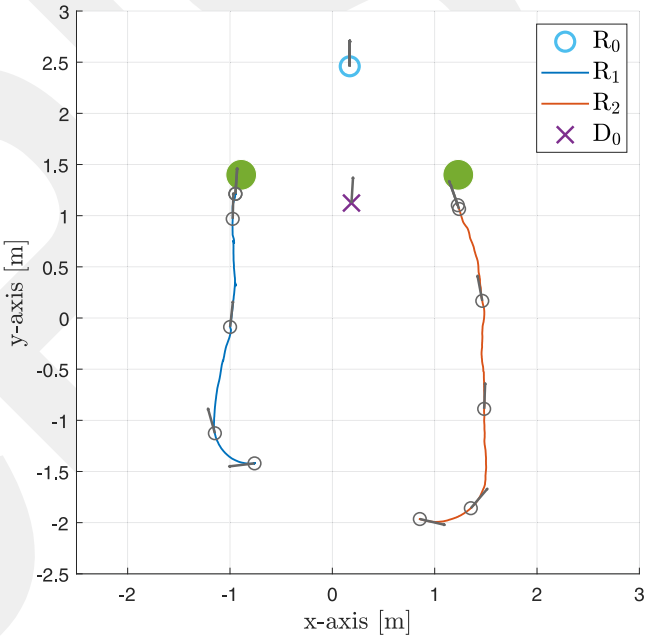

Fig. 16. The traces of the follower UGVs in a formation acquisition experiment (D_0: red cross, R_0: blue circle, R_i, $i = \{1, 2\}$: gray circles; the headings of the robots are shown with gray arrows). The UGVs started from their initial locations with randomly chosen heading angles and aimed at reaching their desired regions indicated by the green colored disks, by utilizing only the UWB distances without measuring their heading angles. (For interpretation of the references to color in this figure legend, the reader is referred to the web version of this article.)

level of errors. Also, the estimation performance improved when the drone tracked the leader R_0 smoothly because otherwise the intended triangle $\{R_i, R_0, D_0\}$ is not formed properly (Fig. 18). The estimation RMSE obtained from six experiments are presented in Fig. 15, which shows that the average estimation error of ϕ_i (0.18 rad) is higher than the estimation error of β_i (0.1 rad). Notably, this result is expected since ϕ_i is not directly measured by the UGVs. Also, the error of ρ_i remained below 0.1 m in all but one experiments. A detailed discussion on the results is provided in Section 9.

8.2. Estimation-based formation acquisition

In the second set of experiments, the formation acquisition controller of Section 6.1 was evaluated. As in the simulation study, the leader UGV R_0 remained stationary, and drone D_0 maintained its configuration behind the UGV R_0 at the height $h = 1.5$ m. Two follower UGVs R_1, R_2 were initiated from well behind the UGV R_0 with random heading angles. The UWB sensors on the robots generated the distance measurements ρ_i, d_i by utilizing the TOF ranging technique, which were broadcast to the ROS network among the robots in real time. The parameter values were set to $\bar{v}_i = 0.15$ m/s, $\rho_{\text{th}} = 0.2$ m, and $k_\omega(t) = \frac{\bar{v}_i}{\delta_i(t)} + 0.5$.

The traces of the UGVs in an experiment are depicted in Fig. 16. It can be observed that the UGVs reached the disks $\mathcal{B}(\mathbf{p}_i^{\text{des}}, \rho_{\text{th}})$ around their desired locations $\mathbf{p}_i^{\text{des}}$ (depicted with the green colored disks). Although UGV R_2 slipped for a short time in the middle of its motion due to a slightly uneven terrain, it could maintain its estimation error bounded and reached its destination. The error variables $\delta_i, \eta_i, e_\beta$ are shown in Fig. 17. As in the simulation results, $\delta_i(t)$ monotonically converge to zero in under 30 sec, and the error variables η_i and the orientation errors e_β remained bounded and converged to a neighborhood of zero. Furthermore, the UGVs R_1, R_2 converged to their desired regions in six other experiments as well, where their initial configurations were not too close to the line l_{0D}, which validated the effectiveness of the approach.

8.3. Estimation-based formation maintaining

In the third set of experiments, the formation controller designed in Section 6.2 together with the estimation algorithm were evaluated. Since the relative heading ϕ_i cannot be measured by the onboard

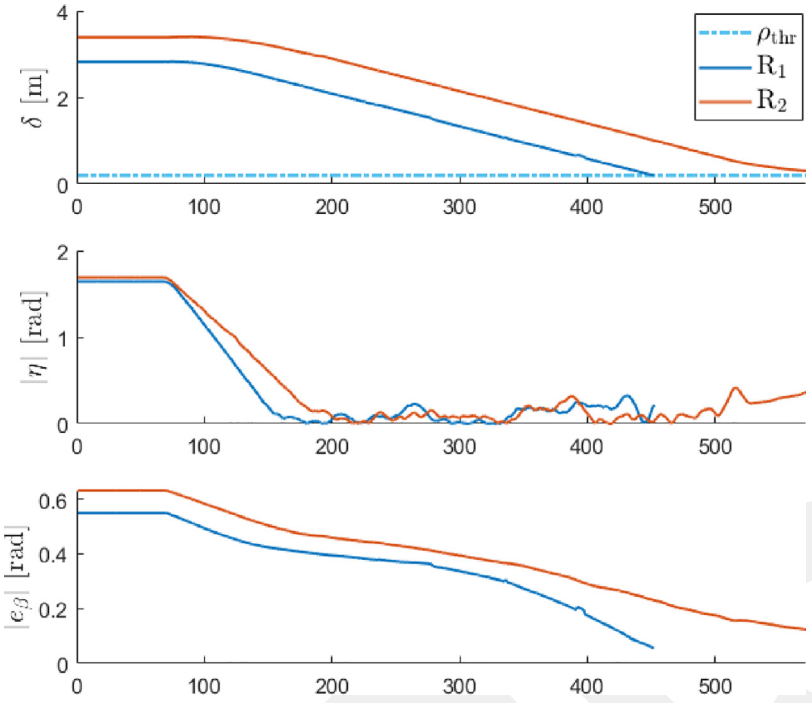

Fig. 17. The error variables in an estimation-based formation acquisition control experiment.

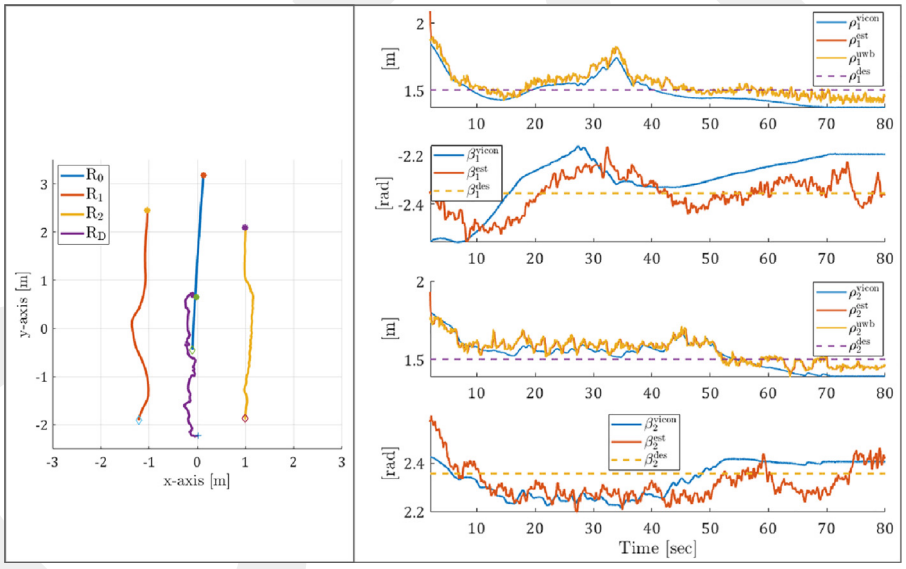

Fig. 18. A formation control experiment: (Left) Traces of the robots; (Right) the relative position estimates.

sensors, the estimated state $\hat{\mathbf{x}}_i = \left[\hat{\rho}_i, \hat{\phi}_i, \hat{\beta}_i\right]^\top$ was used in place of the true variables ρ_i, ϕ_i, β_i. The results of a formation control experiment were illustrated in Fig. 18, where R_1 and R_2 used the control rule (28) to maintain the desired values $\rho_1^{\text{des}} = \rho_2^{\text{des}} = 1.5$ m, $\beta_1^{\text{des}} = -0.75\pi, \beta_2^{\text{des}} = 0.75\pi$ rad toward the leader R_0 which was commanded externally. It was observed that the estimation performance sufficed to maintain the desired formation up to a low error margin. In Fig. 19, the RMSE for the formation errors in six experiments were shown, which are defined as $e^i_{\text{for},\rho} = \left[\frac{1}{K}\sum_{k=1}^{K}\left(\rho_i[k] - \rho_i^{\text{des}}\right)^2\right]^{\frac{1}{2}}$, and $e^i_{\text{for},\beta} = \left[\frac{1}{K}\sum_{k=1}^{K}\left(\beta_i[k] - \beta_i^{\text{des}}\right)^2\right]^{\frac{1}{2}}$, where K is the total time steps during an experiment and i is the follower UGV identity. Although no direct correlation between the error levels and the robots' identities were found, it was observed that the average RMSE remained below 0.15 m for ρ_i and 0.15 rad for β_i, which proves the efficiency of the proposed method. Moreover, an experiment in a relatively large area was conducted, where the robots traveled 12 m path without breaking the formation, video of which can be found in the link.[1]

9. Comparison with the state-of-the-art

In this part, the advantages and constraints of the proposed framework are discussed by comparing it with a selection of the previous works in the literature. The main benefits of the proposed framework are the ability to function in any environment and the low-cost of the onboard sensor suit. Notably, while the relative localization literature contains a vast amount of distance- and vision-based approaches with

[1] https://youtu.be/7mYdhy30zNA

Table 1
A comparison of the proposed approach with the recent literature (RL: Relative localization, GL: Global localization, SR: Scene reconstruction).

Reference	MRS Components	Objective	Sensors Used	Constraints
Saska et al. (2014)	Drones & UGVs	RL	Mono camera on drones	Each UGV must be detected by at least one drone.
Ziegler et al. (2021)	Drones	RL	Stereo camera, UWB	VIO requires enough number of features, no experimental evaluation is provided.
Queralta et al. (2022)	Drones & UGVs	RL & SR	Stereo camera, UWB and LIDAR on UGV, Stereo camera and UWB on drone	Test setup is limited to a UGV and a drone. UGVs must always fly in the FOV of the UGVs
Nguyen et al. (2022)	Drones	RL & GL	Mono camera, IMU, and UWB on each drone	Computational load
Cornejo and Nagpal (2015)	UGVs	RL	Distance sensor on each robot	Collinear robots case, applicability on real hardware
Liu et al. (2019)	UGVs	RL	Stereo camera on each robot	FOV of the stereo cameras, data association, max range of the Kinect stereo.
Ding et al. (2021)	Drones & UGVs	RL	Mono camera	All UGVs must be in the FOV of the drone camera, real-time constraints are not addressed.
Ours	Drone & UGVs	RL	UWB on each robot and a mono camera on the drone	The distance between the leader UGV and the drone needs to be tuned before operation.

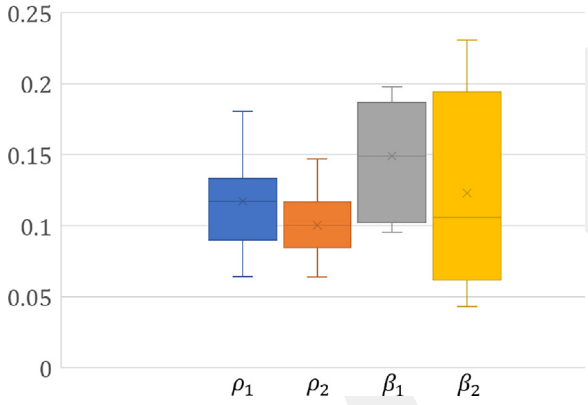

Fig. 19. RMSE of six formation control experiments: ρ_i in meters; β_i in radians.

numerous simulation and experimental analysis, only a few of them used a robotic system similar to the proposed one. Accordingly, a comparison is conducted in terms of not just the precision of the results but also the practicality and efficiency of the systems. A summary of the discussion is given in Table 1. Particularly, the proposed approach is compared with that of Queralta et al. (2022), Saska et al. (2014), Ziegler et al. (2021).

Firstly, a few low-cost onboard sensors suffice to realize the proposed framework, namely a UWB sensor on each robot and a monocular camera on the drone. Thus, it provides cost advantage when compared to HMRS prototypes including other exteroceptive sensors such as 2D/3D LIDARs (Queralta et al., 2022) and stereo cameras (Liu et al., 2019). Although LIDARs and stereo cameras can serve as the fundamental component for global positioning in the absence of external infrastructures, they lead to several issues in local positioning applications featuring the SLAM and visual-inertial odometry (VIO) methods, e.g., high computational load, wrong data association, and poor initialization (Nguyen et al., 2022). The scalable and distributed relative localization approach of Ziegler et al. (2021) also suffers from the disadvantages of the VIO-UWB integration. With the proposed approach, it was demonstrated that a minimalistic sensor suite ($N+2$ UWB sensors and a mono camera) suffices for relative localization in HMRS.

Moreover, inter-robot distance estimation with vision sensors usually perform poor (Kabore & Guler, 2021; Vrba & Saska, 2020). In contrast, the proposed framework utilizes UWB sensors that produce omnidirectional distance measurements and can scale up to more agents at the expanse of slightly reduced data rate. Furthermore, since the proposed framework does not depend on an IMU sensor, its drawbacks, such as long-term drifts and high noise, are eliminated. While IMU sensors can prove useful in a VIO layer for multi-UAV applications (Nguyen et al., 2022; Queralta et al., 2022; Ziegler et al., 2021), the proposed approach eliminates the requirement for IMU and magnetometer by exploiting the unique geometrical properties of its formation graph.

From a computational resource perspective, the proposed distributed framework requires each UGV to run only the standard EKF algorithm at each iteration, which can be achieved by the commercial low-cost computing boards. On the other hand, SLAM or VIO-based frameworks usually require more computational capabilities (Nguyen et al., 2022; Queralta et al., 2022; Ziegler et al., 2021). Also, only the leader UGV velocity should be communicated between the robots in the proposed framework, which can be fulfilled with the UWB sensors onboard.

9.1. Qualitative comparison with vision-only approaches

Typically, vision-only approaches suffer from the limited field-of-view (FOV) of the sensors. In a HMRS, a vision-only solution would require maintaining all UGVs in the FOV of the drone's or the UGVs' cameras, which may perform poorly when the number of the UGVs increase (Cognetti et al., 2014; Krajník et al., 2014; Liu et al., 2019; Saska et al., 2014). For instance, every UGV must be detected by at least one drone in Saska et al. (2014), which puts a significant constraint on the formation shape.

To reflect the proposed framework's advantage over the current vision-based approach of Krajník et al. (2014), Saska et al. (2014) in terms of FOV constraints, a comparative experimental evaluation was conducted. Consider two UGVs as a leader–follower formation and a drone with a downward-facing camera as described in Krajník et al. (2014), Saska et al. (2014). In the purely vision-based approach, both UGVs are equipped with circular patterns on their top sides to be detected by the drone so that the drone's onboard computational unit can calculate and broadcast the relative position between the UGVs. The open-source pattern detection code[2] of Krajník et al. (2014) was

[2] https://github.com/gestom/whycon-orig

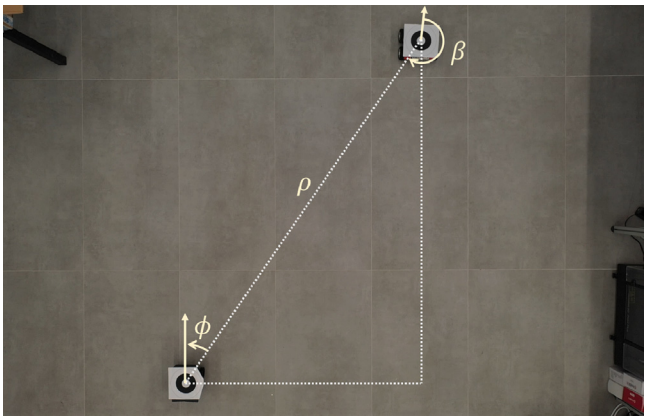

Fig. 20. A sample bird-eye view from the drone camera.

used on the drone images. The circle diameter in the pattern was chosen 12 cm, and an onboard camera with a FOV of 83 × 48 degrees was used on the drone. A sample bird-eye view from the drone's camera at the altitude of 3.7 m is given in Fig. 20 where the inter-UGV distance is $\rho_1 = 2.5$ m. In this image, the two UGVs can be seen clearly, and the patterns and the relative position parameters ρ_i, ϕ_i can be detected with high precision. However, since the UGVs reside at the boundaries of the image, a continuous detection may not be guaranteed while in motion since the UGVs can get out of the image easily. Also, to increase the desired distance ρ between the two UGVs, the drone altitude should be increased. Considering the bounded ceiling heights in indoor environments, flying a drone at the altitude of 3.7 m is not desirable in many scenarios. Alternatively, another drone can be employed to be able to detect both UGVs. Although addition of a drone in the team could solve the detection issue, multi-drone coordination in confined space introduces another research problem. Therefore, the state-of-the-art purely vision-based localization approaches based on a single drone put a restriction on the UGV formation shape and size, and hence, are not scalable.

To reflect the scalability capability of the proposed approach, a series of experiments with both the vision-based approach and the proposed approach on the same robotic setup were conducted. In the vision-based approach, the inter-robot relative configuration was calculated via the classical image processing techniques, and the drone hovered at $h = 2.8$ m which can be considered the maximum reachable safe altitude for most indoor environments. Thus, the vision-based method could detect the UGVs reliably for up to $\rho = 2.2$ m. While evaluating the proposed method, a set of 1000 calibrated distance measurements were processed to generate the distance ρ and the bearing angle β. Fig. 21 illustrates the statistics of the absolute errors $e_\rho = |\rho^{\text{meas}} - \bar{\rho}|, e_\beta = |\beta^{\text{meas}} - \bar{\beta}|$ for both methods, where $\bar{\rho}, \bar{\beta}$ are the true values. It was observed that although the vision-based approach can detect the relative bearing ϕ directly and yields less error magnitude in its function range (i.e., at the altitude of $h = 2.8$ m), it cannot be compared to the proposed approach for $\rho > 2$ m since it was not applicable. It is clearly seen that the proposed approach can yield satisfactory performance for inter-UGV distances of up to $\rho = 5$ m, thanks to its omnidirectional measurement property.

9.2. Estimation algorithms

In Section 5, EKF is applied to estimate the relative poses between the UGVs. Evidently, other estimation schemes can be applied as well because the system is shown to be locally weakly observable. An alternative is the Monte-Carlo localization method, also referred to as a particle filter. As a Bayesian estimation method, a particle filter generates a hypothesis about the state of a system iteratively by employing a set of particles which aim at tracking the state based on the system model. As in the case of the Kalman filter and its variants, these particles are propagated based on a prediction model, which are consequently evaluated in an update (resampling) step. After the resampling step, the particles which have the highest resemblance to the measurements survive while the others are replaced by the surviving particles. At the end of each iteration, the mean of the particles are taken as the state estimation (i.e., the belief). Particle filters can track discontinuous motion and measurement models thanks to their inherent sampling-based characteristics and may outperform the other Bayesian filters in specific scenarios. For instance, in Guler et al. (2021), particle filters yield better performance than the usual EKF due to the agility of the vehicles and discontinuities in the motion and measurement models.

However, particle filters possess several downsides. First, usually a large number of particles are required to be able to track the states. In essence, the performance improves as the number of the particles increases because more particles usually correspond to an increase in the chance of residing in the neighborhood of the actual state values. However, increasing the number of particles requires excessive computational power and increases the epoch time. Second, and more importantly, if the particles are initiated from unsuitable locations, the particles may deviate from the actual state values in the resampling step, which is known as the particle depletion issue. To mitigate the effects of this issue, more particles at random locations can be instantiated at some iterations, but such methods require enormous empirical evaluations and observations on the real system and may not guarantee a reliable estimation.

Finally, particle filters may not offer convergence for unmeasured states. This phenomenon was illustrated on a simulation dataset of Section 7. To track the states (ρ, ϕ, and β) in one of the simulation dataset, the classical particle filter algorithm with 200 particles and the low-variance resampling method were implemented. Fig. 22 shows the estimation performance with the EKF and the particle filter applied. Although the particle filter can track ρ and β with satisfactory performance, it cannot track the unmeasured state ϕ. This is due to the fact that in the resampling phase, the particles whose ρ and β estimations are close to the actual ρ and β values are maintained regardless of the ϕ estimation performance. Thus, the surviving particles do not result in high performance in estimating ϕ.

9.3. Practical issues and limitations

While the proposed framework possesses unique features and outperforms the previous designs in some points, it comes with two limitations. Firstly, if the drone flies close to the leader R_0 on the xy-plane, i.e., if $\bar{d}$ is small, the triangle constructed by the nodes $\{\mathsf{R}_i, \mathsf{R}_0, \mathsf{D}_0\}$ approaches to the collinear case, which causes numerical issues when deriving the angles α_{0i}. Accordingly, the Aruco tag and the drone's camera were mounted obliquely to enlarge the desired distance $\bar{d}$ with reliable tag detection. A detection rate of > 98% was obtained with this design as long as the tag is in the FOV of the camera at take-off. However, it should be noted that this limitation does not restrict the inter-UGV distances ρ_i. The second limitation of the framework stems from the UWB measurement characteristics. The MDEK1001 UWB sensor measurements vary with changing antenna directions between a pair of sensors (as explained in Section 6). Thus, a calibration procedure is required to compute the bias, noise variance, and antenna characteristics of the UWB sensors. Remarkably, the latter limitation is peculiar to UWB sensors and thus applies to all UWB-based approaches, e.g., Kabore and Guler (2021), Nguyen et al. (2022), Ziegler et al. (2021).

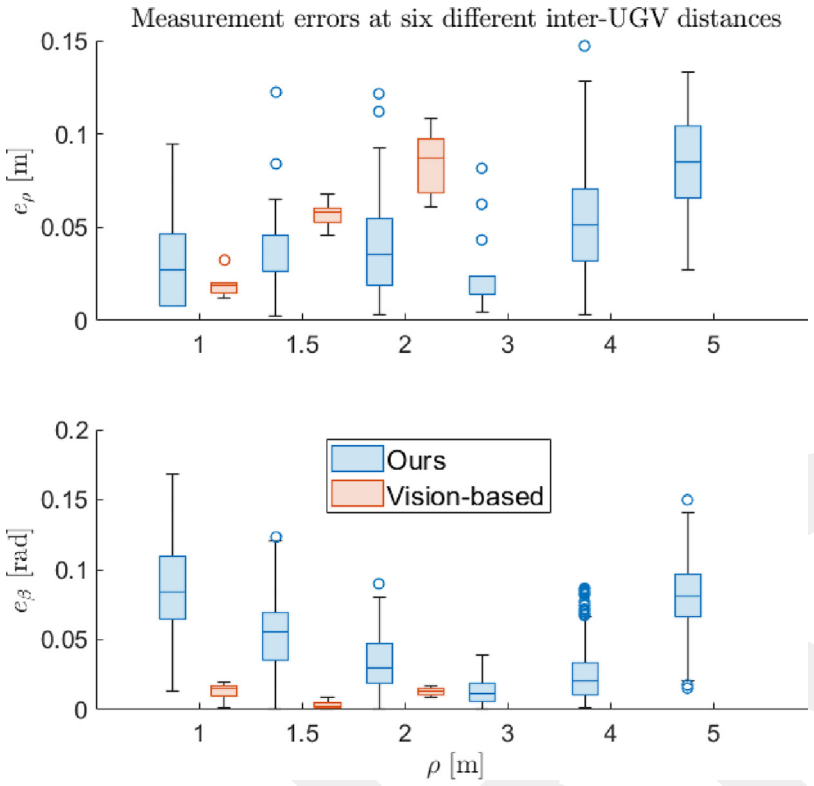

Fig. 21. Comparison with a purely vision-based relative localization approach. The circles stand for the outliers.

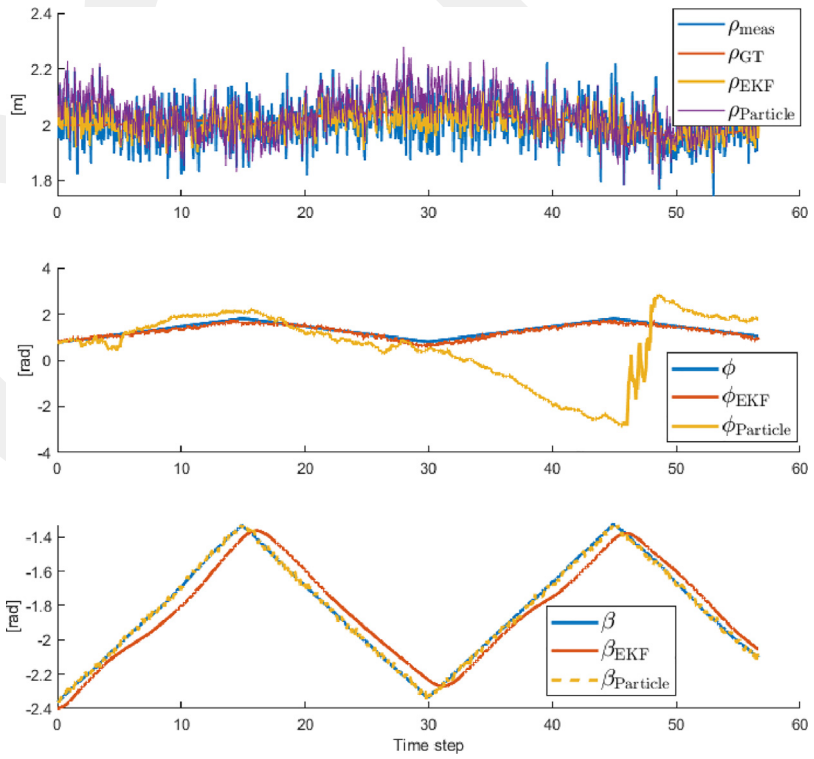

Fig. 22. A comparison of the EKF and the particle filter. While EKF yields satisfactory performance for all three variables, the particle filter cannot track ϕ.

10. Conclusion

The perception algorithm design problem in heterogeneous multi-robot systems consisting of a drone and multiple UGVs have been studied. Motivated by the necessity of a reliable coordination mechanism in challenging environments, a relative localization framework which utilizes ultrawideband sensors and a camera have been proposed, without the need for an absolute sensing aid such as GPS, mocap, and magnetometers. To estimate the relative variables between the UGVs, an EKF algorithm has been designed. Furthermore, the proposed estimation framework has been successfully integrated into two distributed formation control algorithms. A detailed observation analysis on the system model has shown that the unmeasured states are observable under mild assumptions. It has been demonstrated through simulations and real experiments that the proposed method yields sufficient estimation and formation control performance for a variety of applications by removing the tight formation requirement imposed by the vision-only approaches. Possible future directions include realizing the framework with more UGVs and drones and designing robust formation controllers with obstacle avoidance.

Declaration of competing interest

The authors declare that they have no known competing financial interests or personal relationships that could have appeared to influence the work reported in this paper.

Acknowledgments

This paper has been produced benefiting from the 2232 International Fellowship for Outstanding Researchers Program of TÜBİTAK (Project No: 118C348). However, the entire responsibility of the paper belongs to the owner of the paper. The financial support received from TÜBİTAK does not mean that the content of the publication is approved in a scientific sense by TÜBİTAK. The authors thank Ö. Faruk Serin for his help in implementations.

References

Cao, Y., Li, M., Svogor, I., Wei, S., & Beltrame, G. (2018). Dynamic range-only localization for multi-robot systems. *IEEE Access*, *6*, 46527–46537. http://dx.doi.org/10.1109/access.2018.2866259.

Cognetti, M., Oriolo, G., Peliti, P., Rosa, L., & Stegagno, P. (2014). Cooperative control of a heterogeneous multi-robot system based on relative localization. In *2014 IEEE/RSJ international conference on intelligent robots and systems*. IEEE, http://dx.doi.org/10.1109/iros.2014.6942583.

Cornejo, A., & Nagpal, R. (2015). Distributed range-based relative localization of robot swarms. In *Springer tracts in advanced robotics* (pp. 91–107). Springer International Publishing, http://dx.doi.org/10.1007/978-3-319-16595-0_6.

Ding, W., Chen, X., Zhu, W., & Ren, Q. (2021). Vision-based formation control for a heterogeneous multi-robot system. In *2021 IEEE 16th conference on industrial electronics and applications*. IEEE, http://dx.doi.org/10.1109/iciea51954.2021.9516355.

Grocholsky, B., Keller, J., Kumar, V., & Pappas, G. (2006). Cooperative air and ground surveillance. *IEEE Robotics & Automation Magazine*, *13*(3), 16–25. http://dx.doi.org/10.1109/mra.2006.1678135.

Güler, S., Abdelkader, M., & Shamma, J. S. (2019). Infrastructure-free multi-robot localization with ultrawideband sensors. In *2019 American control conference* (pp. 13–18). http://dx.doi.org/10.23919/ACC.2019.8814678,

Guler, S., Abdelkader, M., & Shamma, J. S. (2021). Peer-to-peer relative localization of aerial robots with ultrawideband sensors. *IEEE Transactions on Control Systems Technology*, *29*(5), 1981–1996. http://dx.doi.org/10.1109/tcst.2020.3027627.

Güler, S., Jiang, J., Alghamdi, A. A., Masoud, R. I., & Shamma, J. S. (2018). Real time onboard ultrawideband localization scheme for an autonomous two-robot system. In *2018 IEEE conference on control technology and applications* (pp. 1151–1158). http://dx.doi.org/10.1109/CCTA.2018.8511568,

Güler, S., Yıldırım, I., & Alabay, H. (2022). Mutual relative localization in heterogeneous air-ground robot teams. In *Proceedings of the 19th international conference on informatics in control, automation and robotics*. SCITEPRESS - Science and Technology Publications, http://dx.doi.org/10.5220/0011267800003271.

Hepp, B., Nägeli, T., & Hilliges, O. (2016). Omni-directional person tracking on a flying robot using occlusion-robust ultra-wideband signals. In *2016 IEEE/RSJ international conference on intelligent robots and systems* (pp. 189–194). http://dx.doi.org/10.1109/IROS.2016.7759054,

Hermann, R., & Krener, A. (1977). Nonlinear controllability and observability. *IEEE Transactions on Automatic Control*, *22*(5), 728–740. http://dx.doi.org/10.1109/tac.1977.1101601.

Ioannou, P., & Fidan, B. (2006). *Adaptive control tutorial*. Society for Industrial and Applied Mathematics, http://dx.doi.org/10.1137/1.9780898718652.

Jiménez, A. R., & Seco, F. (2021). Improving the accuracy of decawave's UWB MDEK1001 location system by gaining access to multiple ranges. *Sensors*, *21*(5), 1787. http://dx.doi.org/10.3390/s21051787.

Kabore, K. M., & Guler, S. (2021). Distributed formation control of drones with onboard perception. *IEEE/ASME Transactions on Mechatronics*, 1–11. http://dx.doi.org/10.1109/tmech.2021.3110660.

Kaslin, R., Fankhauser, P., Stumm, E., Taylor, Z., Mueggler, E., Delmerico, J., Scaramuzza, D., Siegwart, R., & Hutter, M. (2016). Collaborative localization of aerial and ground robots through elevation maps. In *2016 IEEE international symposium on safety, security, and rescue robotics*. IEEE, http://dx.doi.org/10.1109/ssrr.2016.7784317.

Khalil, H. K. (2001). *Nonlinear systems*. Prentice Hall.

Kia, S. S., Rounds, S., & Martinez, S. (2016). Cooperative localization for mobile agents: A recursive decentralized algorithm based on Kalman-filter decoupling. In *IEEE control systems IEEE Control Systems*, *36*(2), 86–101. http://dx.doi.org/10.1109/MCS.2015.2512033.

Kim, S. J., & Kim, B. K. (2013). Dynamic ultrasonic hybrid localization system for indoor mobile robots. In *IEEE Transactions on Industrial Electronics IEEE Transactions on Industrial Electronics*, *60*(10), 4562–4573. http://dx.doi.org/10.1109/TIE.2012.2216235.

Klingner, J., Ahmed, N., & Correll, N. (2019). Fault-tolerant Covariance Intersection for localizing robot swarms. *Robotics and Autonomous Systems*, *122*, Article 103306. http://dx.doi.org/10.1016/j.robot.2019.103306.

Krajník, T., Nitsche, M., Faigl, J., Vaněk, P., Saska, M., Přeučil, L., Duckett, T., & Mejail, M. (2014). A practical multirobot localization system. *Journal of Intelligent & Robotic Systems*, *76*(3–4), 539–562. http://dx.doi.org/10.1007/s10846-014-0041-x.

Kushleyev, A., Mellinger, D., Powers, C., & Kumar, V. (2013). Towards a swarm of agile micro quadrotors. *Autonomous Robots*, *35*(4), 287–300. http://dx.doi.org/10.1007/s10514-013-9349-9.

Ledergerber, A., & D'Andrea, R. (2017). Ultra-wideband range measurement model with Gaussian processes. In *2017 IEEE conference on control technology and applications* (pp. 1929–1934). http://dx.doi.org/10.1109/CCTA.2017.8062738,

Li, J., Deng, G., Luo, C., Lin, Q., Yan, Q., & Ming, Z. (2016). A hybrid path planning method in unmanned air/ground vehicle (UAV/UGV) cooperative systems. *IEEE Transactions on Vehicular Technology*, *65*(12), 9585–9596. http://dx.doi.org/10.1109/tvt.2016.2623666.

Liu, X., Ge, S. S., & Goh, C.-H. (2019). Vision-based leader–follower formation control of multiagents with visibility constraints. *IEEE Transactions on Control Systems Technology*, *27*(3), 1326–1333. http://dx.doi.org/10.1109/tcst.2018.2790966.

Liu, C., Zhao, J., & Sun, N. (2022). A review of collaborative air-ground robots research. *Journal of Intelligent and Robotic Systems*, *106*(3), http://dx.doi.org/10.1007/s10846-022-01756-4.

Manyam, S. G., Casbeer, D. W., & Sundar, K. (2016). Path planning for cooperative routing of air-ground vehicles. In *2016 American control conference*. IEEE, http://dx.doi.org/10.1109/acc.2016.7526082.

MBZIRC (2017). URL https://www.mbzirc.com/.

Mueggler, E., Faessler, M., Fontana, F., & Scaramuzza, D. (2014). Aerial-guided navigation of a ground robot among movable obstacles. In *2014 IEEE international symposium on safety, security, and rescue robotics (2014)* (pp. 1–8). http://dx.doi.org/10.1109/SSRR.2014.7017662,

Nguyen, T. H., Nguyen, T.-M., & Xie, L. (2022). Flexible and resource-efficient multi-robot collaborative visual-inertial-range localization. *IEEE Robotics and Automation Letters*, *7*(2), 928–935. http://dx.doi.org/10.1109/lra.2021.3136286.

Prorok, A., Tomé, P., & Martinoli, A. (2011). Accommodation of NLOS for ultra-wideband TDOA localization in single- and multi-robot systems. In *2011 international conference on indoor positioning and indoor navigation* (pp. 1–9). http://dx.doi.org/10.1109/IPIN.2011.6071927,

Queralta, J. P., Li, Q., Schiano, F., & Westerlund, T. (2022). VIO-UWB-based collaborative localization and dense scene reconstruction within heterogeneous multi-robot systems. In *2022 international conference on advanced robotics and mechatronics*. IEEE, http://dx.doi.org/10.1109/icarm54641.2022.9959470.

Roelofsen, S., Gillet, D., & Martinoli, A. (2015). Reciprocal collision avoidance for quadrotors using on-board visual detection. In *2015 IEEE/RSJ International Conference on Intelligent Robots and Systems (IROS)*. IEEE, http://dx.doi.org/10.1109/iros.2015.7354053.

Saska, M., Baca, T., Thomas, J., Chudoba, J., Preucil, L., Krajnik, T., Faigl, J., Loianno, G., & Kumar, V. (2016). System for deployment of groups of unmanned micro aerial vehicles in GPS-denied environments using onboard visual relative localization. *Autonomous Robots*, *41*(4), 919–944. http://dx.doi.org/10.1007/s10514-016-9567-z.

Saska, M., Vonásek, V., Krajník, T., & Přeučil, L. (2014). Coordination and navigation of heterogeneous MAV–UGV formations localized by a 'hawk-eye'-like approach under a model predictive control scheme. *International Journal of Robotics Research*, *33*(10), 1393–1412. http://dx.doi.org/10.1177/0278364914530482.

Staub, N., Mohammadi, M., Bicego, D., Prattichizzo, D., & Franchi, A. (2017). Towards robotic MAGMaS: Multiple aerial-ground manipulator systems. In *2017 IEEE international conference on robotics and automation*. IEEE, http://dx.doi.org/10.1109/icra.2017.7989154.

Tokekar, P., Hook, J. V., Mulla, D., & Isler, V. (2016). Sensor planning for a symbiotic UAV and UGV system for precision agriculture. *IEEE Transactions on Robotics*, *32*(6), 1498–1511. http://dx.doi.org/10.1109/tro.2016.2603528.

Vidal, R., Shakernia, O., Kim, H., Shim, D., & Sastry, S. (2002). Probabilistic pursuit-evasion games: theory, implementation, and experimental evaluation. *IEEE Transactions on Robotics and Automation*, *18*(5), 662–669. http://dx.doi.org/10.1109/tra.2002.804040.

Vrba, M., & Saska, M. (2020). Marker-less micro aerial vehicle detection and localization using convolutional neural networks. *IEEE Robotics and Automation Letters*, *5*(2), 2459–2466. http://dx.doi.org/10.1109/lra.2020.2972819.

Wallar, A., Araki, B., Chang, R., Alonso-Mora, J., & Rus, D. (2018). Foresight: Remote sensing for autonomous vehicles using a small unmanned aerial vehicle. In M. Hutter, & R. Siegwart (Eds.), *Field and service robotics* (pp. 591–604). Cham: Springer International Publishing.

Wang, C., Zhang, H., Nguyen, T. M., & Xie, L. (2017). Ultra-wideband aided fast localization and mapping system. In *2017 IEEE/RSJ International conference on intelligent robots and systems* (pp. 1602–1609). http://dx.doi.org/10.1109/IROS.2017.8205968,

Yu, H., Meier, K., Argyle, M., & Beard, R. W. (2015). Cooperative path planning for target tracking in urban environments using unmanned air and ground vehicles. *IEEE/ASME Transactions on Mechatronics*, *20*(2), 541–552. http://dx.doi.org/10.1109/tmech.2014.2301459.

Ziegler, T., Karrer, M., Schmuck, P., & Chli, M. (2021). Distributed formation estimation via pairwise distance measurements. *IEEE Robotics and Automation Letters*, *6*(2), 3017–3024. http://dx.doi.org/10.1109/lra.2021.3062347.